# Empirical single-cell tracking and cell-fate simulation reveal dual roles of p53 in tumor suppression

Ann Rancourt[1,2], Sachiko Sato[1,3,4], and Masahiko S. Satoh[2,3,4]*

[1]Glycobiology and Bioimaging Laboratory of Research Center for Infectious Diseases and Research Centre of CHU de Québec, [2]Laboratory of DNA Damage Responses and Bioimaging, Research Centre of CHU de Québec, [3]The Bioimaging Platform of Research Centre of CHU de Québec and [4]Faculty of Medicine, Laval University, 2705 Boulevard Laurier, Québec, G1V 4G2, Canada

Corresponding author: Masahiko S. Satoh

TEL: 1-418-525-4444 ext. 47340

FAX: 1-418-654-2159

e-mail: masahiko.sato@crchudequebec.ulaval.ca

**ABSTRACT**

The tumor suppressor p53 regulates various stress responses via increasing its cellular levels. The lowest p53 levels occur in unstressed cells; however, the functions of these low levels remains unclear. To investigate the functions, we used empirical single-cell tracking of p53-expressing (Control) cells and cells in which p53 expression was silenced by RNA interference (p53 RNAi). Here we show that p53 RNAi cells underwent more frequent cell death and cell fusion, which further induced multipolar cell division to generate aneuploid progeny. Those results suggest that the low levels of p53 in unstressed cells indeed have a role in suppressing the induction of cell death and the formation of aneuploid cells. We further investigated the impact of p53 silencing by developing an algorithm to simulate the fates of individual cells. Simulation of the fate of aneuploid cells revealed that these cells could propagate to create an aneuploid cell population. In addition, the simulation also revealed that more frequent induction of cell death in p53 RNAi cells under unstressed conditions conferred a growth disadvantage compared with Control cells, resulting in faster expansion of Control cells compared with p53 RNAi cells, leading to Control cells predominating in mixed cell populations. In contrast, growth of Control cells, but not p53 RNAi cells, was suppressed when the damage response was induced, allowing p53 RNAi cells to gain a growth advantage over Control cells. These results suggest that, although p53 could suppress the formation of aneuploid cells, which could have a role in tumorigenesis, it could also allow the expansion of cells lacking p53 expression when the damage response is induced. p53 may thus play a role in both the suppression and the promotion of malignant cell formation during tumorigenesis.

## INTRODUCTION

The p53 gene is mutated in > 50% of cancers [1-3], and loss of p53 function is considered to be involved in tumor progression, thereby defining *TP53* as a tumor suppressor gene [4, 5]. The cellular functions mediated by p53 are mainly related to its cellular levels, which increase in response to stress, thus activating various mechanisms e.g. cell cycle arrest, cell senescence, cell death, and DNA damage responses [5-9]. Given that cell cycle arrest, cell senescence and cell death could lead to removal of the damaged cells, these processes could act to suppress tumor formation [6, 10-15].

p53 levels are regulated via a mechanism mediated by Mdm2, which constantly degrades p53 by ubiquitination to maintain a low level. p53 accumulation occurs when Mdm2 activity is suppressed by stress-induced phosphorylation, which inhibits its ubiquitination activity, resulting in inhibition of p53 degradation [4, 6, 7, 16-18]. These observations suggest that increased stress levels are required to elevate p53 levels sufficiently to allow it to exert its tumor suppressor function. Maintaining a background low level of p53 may thus have evolved as a means of allowing cells to respond quickly to stress. Alternatively, given that removing p53 by gene silencing increases the efficiency of induced pluripotent stem cell formation [19], maintaining low levels of p53 in unstressed cells *per se* may have functional implications. With this regard, it has been suggested that low levels of p53 activity may require normal cell growth to respond to a broad spectrum of stress [20] through suppression of apoptosis and regulation of metabolisms [4, 6, 21, 22]. If low levels of p53 indeed play a role in regulating cellular functions, it is plausible that loss of these functions could be involved in tumorigenesis. However, the effects of loss of low levels of p53 on cell characteristics remain unclear.

In this study, we investigated the effects of loss of low levels of p53 on the frequency of induction of various cellular events using single-cell tracking, to create a cell-lineage database and lineage maps. In contrast to lineage-reconstruction approaches that assume that all cell divisions are bipolar [23-25], single-cell tracking can detect other types of cellular events, e.g. cell death, multipolar cell division, and cell fusion, allowing the generation of accurate cell lineage data. In this study, we used the

alkylating agent, *N*-methyl -*N'*-nitroso-*N*-nitrosoguanidine (MNNG), which generates methylated bases, to increase p53 levels in cells [26, 27]. Among MNNG-induced methylated bases, $O^6$-methylguanine acts as a premutagenic DNA lesion that induces a G:C to A:T transversion mutation, and 7-methylguanine causes the induction of cell death through the formation of DNA breaks, produced during the repair of 7-methylguanine by base excision repair [28-32]. Thus, cells may respond to MNNG by p53-related mechanisms, but other mechanisms are also induced in response to MNNG exposure. We used data obtained by single-cell tracking to develop a cell-fate simulation algorithm. Our results suggest that the low levels of p53 in unstressed cells play a role in suppressing the induction of cell death and cell fusion, which may lead to multipolar cell division and the production of aneuploid progeny. Cell-fate simulation analysis revealed that some aneuploid progeny derived from p53-silenced (p53 RNAi) cells could propagate in an environment dominated by p53-expressing (Control) cells, while p53 RNAi cells *per se* were unable to gain a growth advantage over Control cells. In contrast, the growth balance between Control and p53 RNAi cells was altered by induction of the damage response by MNNG, resulting in the relative expansion of p53 RNAi cells. Thus, although low levels of p53 could act as a tumor suppressor by inhibiting the formation of aneuploid cells, this role could largely depend on the status of the cell population harboring the cells with impaired p53 function, and the environment of the stress-damaged population.

## RESULTS

### System to investigate the functional implications of maintaining low levels of p53 in unstressed cells

We developed a system to determine if the low levels of p53 retained in unstressed cells had a functional role in suppressing changes in cell characteristics. We therefore performed concurrent video recording of A549 p53 proficient lung carcinoma cells treated with scrambled small interfering RNA (siRNA) or p53 siRNA (Control and p53 RNAi cells, respectively), and analyzed spatiotemporal changes in individual cells using single-cell tracking. Particularly, we selected the transient silencing approach to minimize the involvement of other factors, e.g. phenotypical alterations accumulating occurred during the maintenance of culture. We also monitored the responses of the Control and p53 RNAi cells to MNNG. Concurrent video recording was performed using differential interference contrast (DIC) imaging with near-infrared light to minimize cytotoxicity. To generate a video that recorded continuous cell movement, images of typically 2,300 × 2,300 pixel area (1,200 × 1,200 μm) were acquired every 10 min (Figure 1). To start single-cell tracking, cells referred to as progenitors were selected in video images at a tracking time of 0 min, and single-cell tracking of progenitors and their progeny was performed by identifying cellular events including bipolar cell division, tripolar cell division, tetrapolar cell division (tripolar and tetrapolar cell divisions were defined as multipolar cell division), cell death, and cell fusion (see Figure 1-figure supplement 1 for still images of bipolar cell division, multipolar cell division, cell death and cell fusion; corresponding videos have been deposited in Dryad). We developed a computerized single-cell tracking analysis system[33] to generate a cell-lineage database suitable for quantitative bioinformatics analysis (Figure 1). Notably, if a progenitor or any of its progeny moved out of the field of view, data related to those cells were not included in the cell-lineage database. A unique ID, referred to as a cell-lineage number, was assigned to each progenitor and the progeny derived from that progenitor was identified based on the ID. The cell-

lineage database thus included the cell-lineage number, cell number, position of a cell, type and time of events that occurred in a cell, and the relationships of a cell to its parent and offspring cells.

We also created cell-lineage maps to visually represent the fates of cells with the same cell-lineage numbers (cells derived from the same progenitor) (Figure 1). The map contained multidimensional information, e.g. number of progeny produced from a progenitor, type and time of events that occurred in a cell or in all cells comprising the lineage, and the length of time between events. Quantitative bioinformatics analyses were performed by focusing on specific aspects of this information, and statistical analysis was performed with all cell-lineage data recorded in the cell-lineage database or by selecting certain types of cell lineages. Furthermore, given that spatiotemporal information on individual cells can reveal a pattern of events that occurred in the cell, cell-lineage, and cell population, we also used the information to simulate the fates of cells by developing a cell-fate simulation algorithm.

**Culture of A549 cells**

There is currently no standard protocol for single-cell tracking analysis using RNA interference. We therefore examined some critical experimental parameters. First, we prepared uniform cell cultures for siRNA treatment using plated cells occupying ~90% of the culture surface, where > 99% of cells were attached to other cells. Although A549 could show a relatively linear growth pattern through various cell densities, this condition may cause over-confluency of cells. However, as shown in Figure 1-figure supplement 2a, the number of cells /$\mu m^2$ increased linearly while the average cell surface area was reduced, confirming that these cells could continue to grow during video monitoring at this density. To visualize this cell density increase, density maps were also created at each imaging time point (Figure 1-figure supplement 2b for still images and Figure 1-video 1) by assigning a value of 1 to pixels within a 20-pixel diameter (10.43 µm) of the position of the cell (Figure 1-figure supplement 2c). Cell positions were determined using data recorded in the cell-lineage database, and if an area overlapped

with other areas, the pixel was assigned the sum of the number of overlapped areas. These values that reflect cell density were converted into a heat map, which showed an increase in density during video monitoring (Figure 1-figure supplement 2b and Figure 1-video 1).

**Minimum number of cell-lineages required to build a cell-lineage database**

We also determined the minimum number of cell-lineages (i.e. number of progenitors to be tracked) needed per experimental condition to build a cell-lineage database with reproducible results. We first performed single-cell tracking using 485 progenitors and then reconstructed cell-lineage databases with 50–240 cell-lineages by random selection. For example, 50 cell lineages were randomly selected from 485 cell lineages to build a cell-lineage database, and this selection was repeated three times for triplicate analysis. Cell population expansion curves were then generated to assess analytical variation. The results for 50, 80, 120, 140, and 240 cell-lineages are shown in Figure 1-figure supplement 3a-e. Plotting growth variation at a tracking time of 4,000 min showed that the variations tended to a constant (7.5–6.0 for 150–240 cell lineages) when >240 cell-lineages were used (Figure 1-figure supplement 3f). This suggests that 240 cell-lineages are sufficient for reproducible single-cell tracking analysis, and we therefore used 335 cell-lineages to create a cell-lineage database.

**Silencing of p53 and single-cell tracking**

We determined the length of time required for single-cell tracking following siRNA transfection. Because transfection can be monitored by observing the accumulation of particles (transfection reagents) in cells (Figure 1-figure supplement 4a, DIC), we quantitated the number of particles in an area of the cell culture by extracting particles with a grayscale value >150/255 from the video image, and counted the number of particles with a size of 5–30 pixels (Figure 1-figure supplement 4a, Particles, and Figure 1-video 2). The number of particles started to increase at about 1,200 min (20 h) after transfection and peaked at 3,750 min (62.5 h) (Figure 1-figure supplement 4b). Western blotting

analysis performed 48 h after transfection confirmed silencing of p53 (Figure 1-figure supplement 4c; Scrambled siRNA *vs.* p53 siRNA, ~70% reduction), the expression of low levels of p53 (Scrambled siRNA, 0 μM MNNG) and the occurrence of p53 stabilization by exposure of cells to 7 μM MNNG (Scrambled siRNA, 5.8-fold increase). Based on these parameters, we applied a 30-min pulse of MNNG treatment after the start of particle accumulation (Figure 1-figure supplement 4b; 1,740 min (29 h) after transfection). Single-cell tracking was started at the end of MNNG treatment and continued for 4,000 min (66.7 h), by which time the number of particles was reduced to 70% of that at the peak.

Notably, the degree of p53-silencing may vary among cells, and it is possible that only certain groups of cells may respond to silencing. However, there is currently no technique available for accurately quantitating the levels of p53 in unstressed individual cells and relating the levels to the single-cell tracking data. We were therefore unable to reveal the relationship between the degree of silencing and the responses of individual cells to silencing. However, if a response occurred in a certain group of cells, it would provide a clue to the function of the low levels of p53.

**Effect of silencing the low levels of p53 on cell population expansion**

The lowest levels of p53 could occur in unstressed cells [4, 6, 7, 16-18]. To gain insights into the functions of such low levels of p53, we analyzed the expansion rate of a p53 RNAi cell population and their response to MNNG exposure. The rate of cell population expansion or cell growth has generally been measured by counting cells at certain intervals. We therefore initially determined the expansion curves using a cell-counting approach (count cell numbers every 1,000 min) and compared the results with those obtained by single-cell tracking analysis (every 10 min), to evaluate the accuracy of the single-cell tracking analysis (Figure 2). We determined the expansion curves using a counting approach based on live-cell imaging videos. To this end, images corresponding to every 100 time points (1,000 min) were divided into 5 × 5 squares (~512 × 512 pixels per square, 266.24 × 266.24 μm per square) and the number of cells within a square was determined (Figure 2-figure supplement 1). We used three

independently generated videos with multiple squares from each. The results of counting of Control and p53 RNAi cells are summarized in Figure 2a and b, respectively. The rates of expansion of the Control and p53 RNAi cells and their responses to MNNG exposure were also compared (Figure 2c-f). There was no significant difference in the expansion rates of Control and p53 RNAi cells (Figure 2c). There was also no significant difference in the expansion rates of Control cells and Control cells exposed to 1 μM MNNG (MNNG1) (Figure 2a, Control vs. MNNG1), while the expansion rate of p53 RNAi cells exposed to 1 μM MNNG (p53 RNAi-MNNG1) was reduced relative to Control cells exposed to MNNG1 (MNNG1) and p53 RNAi cells (Figure 2b and d). When the dose of MNNG was increased to 3 μM (MNNG3), the expansion rate of MNNG3 cells was reduced relative to Control cells (Figure 2a), but was higher than that of p53 RNAi-MNNG3 cells (Figure 2e, MNNG3 and p53 RNAi-MNNG3). At the highest MNNG dose used in this study (7 μM, MNNG7) at which dose significant accumulation of p53 was observed (Figure 1-figure supplement 4c), the rates of expansion of both the MNNG7 and p53 RNAi-MNNG7 cell populations were significantly reduced compared with non-exposed Control and p53 RNAi cells, respectively, but p53 RNAi cells were significantly less sensitive to the MNNG dose than Control cells (Figure 2f). These results suggest that cells with different sensitivities to MNNG compared with Control cells were generated by silencing the low levels of p53. Furthermore, the relative sensitivities of Control and p53 RNAi cells to different doses of MNNG differed, further suggesting that these cells did not respond linearly to the different doses of MNNG.

We then compared the results obtained by cell counting with those obtained by computer-assisted single-cell tracking analysis to verify whether this analysis indeed yields results consistent with the classical counting method. Because the cell-lineage database generated by tracking contained information on individual cells at each time point in the images (every 10 min), the total number of cells at every 10 min was plotted in Figure 2g-l (videos of the single-cell tracking processes, cell lineage maps, and cell lineage data have been deposited in Dryad). Indeed, single-cell tracking analysis and cell counting yielded similar results (Figure 2g and h); the relative differences in the rates of cell

expansion between the Control and p53 RNAi cells, and these treated with MNNG, were consistent between the counting and single-cell tracking results (Figure 2j-l). Regarding the comparison between Control and p53 RNAi cells, although counting every 1000 min showed no significant differences, single-cell tracking revealed that the population expansion rate of p53 RNAi cells was significantly lower than that of Control cells, confirming the sensitivity of this analysis than classical counting method (Figure 2c and i). Nevertheless, these results indicated that single-cell tracking analysis could determine the growth of a cell population with similar accuracy to a cell-counting approach. However, in contrast to the counting approach, which only represents the number of cells at a certain time point, information on individual cells obtained by single-cell tracking was associated with spatiotemporal information that could allow a more detailed analysis of how the cell population is formed and responds to DNA damage stress. We therefore conducted further analyses to gain insights into the Control and p53 RNAi cell populations and those exposed to MNNG using computer-assisted single-cell analysis.

**Analysis of cell population at the cell-lineage level**

Cell populations are known to be composed of cells with different reproductive abilities [34], and the overall rate of cell population expansion shown in Figure 2 is thus often influenced by the relative reproductive abilities of the cells that constitute the population. However, cell population expansion curves *per se* do not provide any insights regarding the reproductive abilities of individual cells. We therefore analyzed the reproductive abilities of the different cells comprising the cell population, to understand the formation of the Control, p53 RNAi, and MNNG-exposed cell populations.

To this end, we sorted each cell lineage into groups (Figure 3a). Given that the reproductive ability of a cell could be represented by the number of progeny present at a certain moment in time, we analyzed each cell lineage and sorted it according to the number of progeny cells at 4,000 min of culture (in the example cell lineage shown in Figure 3a (left), three cells were present at 4,000 min). We grouped

progenitors that produced 1–3, 4–6, 7–9, 10–12, and 13–15 progeny cells at 4,000 min as Groups A, B, C, D, and E, respectively. The lineages in Figure 3a left and right were therefore sorted as Groups A and B, respectively.

The total numbers of progeny cells at 4,000 min in the different groups are shown in Figure 3b. In the case of Control cells, most cell-lineages belonged to Group C, which accounted for 51% of the progeny at 4,000 min. Most p53 RNAi cell lineages also belonged to Group C, but the number of cells with higher reproductive capacity, i.e. Group D, was increased relative to Control cells (143 cells *vs* 33 cells, respectively), which might represent a change induced by silencing the low levels of p53. The number of cell lineages in Group C was increased in the MNNG1 compared with the Control population (1111 cells *vs* 915 cells), but the number of corresponding lineages in p53 RNAi-MNNG1 cells was reduced (623 cells *vs* 1111 cells). This difference may reflect the difference in cell population-expansion rates between MNNG1 and p53 RNAi-MNNG1 cells (Figure 2j). Because MNNG is a cytotoxic agent, it could reduce the number of cells with a higher reproductive ability and increase cells with a lower reproductive ability. Indeed, the numbers of Group A cell lineages were increased in MNNG3 and p53 RNAi-MNNG3 cells, but MNNG3 cells could maintain a higher ability to expand relative to p53 RNAi-MMNG3 cells, because of the higher content of Group C cell lineages (708 cells *vs* 444 cells). Most lineages in MNNG7 and p53 RNAi-MNNG7 cells were Group A. However, p53 RNAi-MNNG7 cells still included Group C lineages, which could allow the cell population to recover from the impact of 7 μM MNNG treatment. These results suggest that the Control cells did not respond to different doses of MNNG in a simple dose-response manner, and that silencing the low levels of p53 also differentially affected the response patterns. Multipolar cell division, cell death, and cell fusion are also likely to be involved in determining the response patterns, and we therefore further analyzed the impact of p53-silencing and MNNG exposure on those events.

**Impact of p53-silencing and MNNG treatment on cell death, multipolar cell division and cell fusion**

Multipolar cell division occurs at a low frequency of 1%–10% of all cell divisions[35, 36]. Cell death also occurs at a low frequency, except in the presence of a cytotoxic agent. Although cell fusion is often induced during differentiation, e.g. myogenesis, it is rarely induced in a growing cell population. In general, the accuracy of detecting a low-frequency event is lower than that for frequently occurring events, e.g. bipolar cell division. We therefore determined if single-cell tracking could detect multipolar cell division, cell death, and cell fusion with adequate accuracy for statistical analysis. To this end, we determined the number of multipolar cell division and cell death events visually by manual counting in videos, and compared the results with those obtained using single-cell tracking analysis (Figure 4). Notably, cell fusion was not included in the counting analysis because it was difficult to detect without single-cell tracking.

For counting, each time point of the video image was divided into four squares (Figure 4-figure supplement 1a), and cell death and multipolar cell division events were marked. Figure 4a and b as well as Figure S6b and c showed that p53 silencing significantly increased multipolar cell division and cell death events relative to Control cells. This suggested that, even though Control and p53 RNAi cells showed similar cell population expansion curves (Figure 2i), the sizes of the p53 RNAi and Control cell populations were determined by different processes. Increased multipolar cell division and cell death events following p53 silencing were significantly reduced by MNNG treatment (Figure 4a, b, S6b and c), with the degree of suppression of multipolar cell division being more significant than that of cell death. Multipolar cell division and cell death occurred less frequently in Control cells, even after exposure to MNNG, except for cells exposed to 7 μM MNNG (Figure 4b). These results suggest that silencing of the low levels of p53 led to the induction of multipolar cell division and cell death, which are not necessarily well-reflected in cell population expansion curves.

Even though single-cell tracking analyzed cells located in a certain area of the culture (Figure 4-figure supplement 1b and c, black box), which was smaller than manual counting, analyses of multipolar cell division and cell death by computer-assisting tracking yielded results that were consistent with the counting approach (Figure 4a-b *vs.* c-d). In one case, i.e. treatment of cells with 7 μM MNNG, the number of cell death events in Control cells determined by counting was higher than that determined by single-cell tracking analysis. This was because the area of single-cell tracking was slightly outside the area where cell death frequently occurred (Figure 4-figure supplement 1c). However, given that such events do not occur with the same probability throughout the field of view, some variation may occur with both the counting and single-cell tracking approaches. We thus concluded that single-cell tracking analysis could accurately detect the occurrence of multipolar cell division and cell death in a cell population. Finally, we analyzed cell fusion, which required the fused cells to be followed for at least 30 time points (~5 h), necessitating the use of single-cell tracking analysis. Similar to multipolar cell division and cell death, p53 silencing increased the frequency of cell fusion, and this was counteracted by MNNG (Figure 4e). The chances of detecting multipolar cell division, cell death, and cell fusion in p53 RNAi cells at a certain time point in an image were 0.014, 0.037, and 0.023/hour/100 lineages, respectively (for Control cells, 0.001, 0.004 and 0.004/hour/100 lineages), confirming the relatively lower frequencies of these events relative to bipolar cell division (0.54/hour/100 lineages).

### ***In silico* generation of a cell-lineage database of p53 RNAi cells**

Despite the similar cell population expansion curves of p53 RNAi and Control cells (Figure 2), detailed analyses of the cell behaviors revealed that silencing the low levels of p53 resulted in increased multipolar cell division, cell death, and cell fusion (Figure 4). This may be because the less frequent occurrence of cell death in p53 RNAi cells relative to bipolar cell division (0.037 *vs.* 0.54/hour/100 lineages, respectively) did not affect the overall rate of expansion. Alternatively, silencing promoted the reproductive ability of certain subsets of the p53 RNAi cell population, such as group D cell

lineages (Figure 3b), but the silencing-induced increases in multipolar cell division, cell death, and cell fusion may counteract the increased reproductive ability. In particular, cell death could have a significant impact on reducing the cell population size. In the example in Figure 5a, cell death reduced the number of progeny by half. To determine if the induction of cell death could indeed affect the rate of cell population expansion, we generated an *in silico* cell-lineage database, assuming no cell death (Figure 5a). Cell-lineage data terminated by cell death were replaced with cell-lineage data for its sibling, based on an assumption that if the cell continued to grow, its growth was most likely to be similar to that of its sibling. If both siblings underwent cell death, both cells were assumed to survive until the end of the analysis. The cell population expansion rate of the *in silico*-generated p53 RNAi cells without cell death (p53 RNAi-Silico(-)cell death) (Figure 5b) showed that cell death led to a 7.4% reduction in the cell population size at a tracking time of 4,000 min (Figure 5b; p53 RNAi *vs.* p53 RNAi-Silico(-)cell death). The estimated cell population size of the p53 RNAi-Silico(-)cell death cells was larger than those of the Control and *in silico*-generated Control cells (Control-Silico(-)cell death). These results suggest that p53 silencing promoted the reproductive ability of p53 RNAi cells, but this was counteracted by the induction of cell death, resulting in the formation of p53 RNAi cell populations that were smaller than Control cell populations (Figure 2i). This analysis also shows that the effect of silencing the low levels of p53 cannot be detected without access to the spatiotemporal information on individual cells provided by single-cell tracking.

**Events leading to multipolar cell division**

Multipolar cell division and cell fusion could have greater impacts than cell death in terms of creating diversity in the cell population, by causing the formation of aneuploid cells[37-42], if the progenies of multipolar cell division or cell fusion events survive. We further examined how silencing the low levels of p53 altered the characteristics of cells by focusing on multipolar cell division and cell fusion and the relationships between these events. To this end, we used cell-lineage maps to identify cells that

underwent multipolar cell division, and traced back along the map to find an event that occurred prior to the division (Figure 6a). We identified two patterns: multipolar cell division occurring after cell fusion (Pattern 1: Cell fusion ➛ Multipolar cell division), and multipolar cell division without cell fusion (Pattern 2: Multipolar cell division). Following cell fusion, Control and p53 RNAi cells demonstrated 79.4% and 93.2% multipolar cell divisions, respectively, and it is likely that cells with increased ploidy could have a higher chance of undergoing multipolar cell division. Notably, these results suggest that p53 silencing induced multipolar cell division by promoting the chance of cell fusion (Pattern 1). We then analyzed cells that fused by tracing further back along the cell-lineage maps (Figure 6b). Interestingly, cell fusion was more frequent between sibling cells (Pattern 3). In this regard, a previous study reported that some persistent link remained after bipolar cell division leading to cell fusion [43]. However, given that cell fusion also occurred between non-siblings (Pattern 4), the cell fusion observed in this study may have been mediated by other processes. Nevertheless, p53 silencing mainly promoted the sequence of events: Bipolar cell division ➛ Cell fusion between siblings ➛ Multipolar cell division (Figure 6b, Pattern 3).

The progeny of multipolar cell division have been reported to be fragile, although some are capable of entering a growth cycle [39, 40]. We, therefore, analyzed the survival of the progeny using cell-lineage maps. In terms of percentage survival, 3.2%–3.6% of the total number of progeny produced by multipolar cell division survived in both Control and p53 RNAi cells (Figure 6c). On the other hand, given that silencing the low levels of p53 *per se* increased the number of multipolar cell divisions, the number of surviving cells in the p53 RNAi cell population was increased 10.1-fold (0.61 progeny of multipolar cell division/100 cell lineages of p53 RNAi cells vs. 0.06 progeny of multipolar cell division/100 cell lineages of Control cells). These results suggest that p53 silencing mainly promoted the sequence of events: Bipolar cell division ➛ Cell fusion between siblings ➛ Multipolar cell

division ➛ Survival of aneuploid progeny, leading to the creation of genetic diversity in the p53 RNAi cell population.

These results also suggest that increasing the frequency of bipolar cell division would increase the frequency of multipolar cell divisions, while reducing the number of bipolar cell divisions by exposure to MNNG would also reduce multipolar cell divisions. Indeed, plotting the number of bipolar cell divisions against the number of multipolar cell divisions in p53 RNAi cells (Figure 6d) showed direct proportionality. These results suggest that MNNG indirectly reduced the number of the events in the sequence: Bipolar cell division ➛ Cell fusion between siblings ➛ Multipolar cell division ➛ Survival of aneuploid progeny. Although MNNG is a mutagen that induces G-T to A-T transversion mutations through the formation of $O^6$-methylguanine[26], it could act to suppress the formation of aneuploid cells in some contexts, with possible relevance to the development of cancer[44].

**Cell-fate simulation algorithm**

The above data suggest that the fate of cell progeny following silencing of the low levels of p53 could alter the characteristics of the cells and their sensitivity to MNNG. However, characterization of the cells using an empirical approach was limited by culture-related factors, e.g. cell confluency. To overcome this limitation and further analyze the effects of p53 silencing on the fate of the cell population, we utilized the spatiotemporal information for each cell in the cell-lineage database records, which revealed the cell's relationships with its parents, siblings, and offspring, and events that occurred in that cell. This spatiotemporal information provided a growth pattern for each cell lineage and cell population. We then used this information to develop an algorithm to simulate the fate of cells to overcome the limitations associated with empirical approaches.

This simulation required an algorithm to generate virtual cell-lineage data. The underlying concept of the cell-fate simulation algorithm is shown in Figure 7 (details in Figure 7-figure supplement 1). We

first decomposed a cell lineage into units sandwiched between two events, such as bipolar cell division, multipolar cell division, cell fusion, and cell death (Figure 7a). We referred to events that initiated and ended the unit as Start and End events, respectively, and each unit was thus defined by the nature of its Start and End events, and the length of time between the two events. An algorithm combining such units can thus be used to generate a virtual cell lineage with a similar pattern to an empirically determined lineage. Because each cell lineage in a cell population shows a variety of patterns, and this variation defines the characteristics of the cell population, the simulation algorithm thus needs to reflect this variation. To this end, we first produced a series of histograms of the distribution of the end events for each Start event (Figure 7b). For example, if the Start event was bipolar cell division, we created a histogram of the frequency of all possible End events, i.e. bipolar cell division, multipolar cell division, cell death, and cell fusion. We referred to the histogram data as Operation data-Events. The algorithm then reflected this distribution to choose the End event. Once the Start and End events were chosen, the algorithm referred to another set of histograms (Operation data-Time), which showed the distribution of the length of time for a given unit (Figure 7c). For example, for a unit with bipolar cell division as the Start event and cell fusion as the End event, the algorithm referred to the histogram of time length distributions of the corresponding event combination. These processes were repeated until the cell lineage reached the desired time point. In addition to the process of assigning event type and time length, a cell doubling time of parent cell was taken into account. If both the first start and second end events of a parent cell were bipolar cell division, the length of time of its offspring was limited to generally ± 10% of that of the parent cell. If a parent cell has a shorter length of time, than others, its progeny also could have a shorter doubling time, creating an actively growing cell lineage. In this manner, the algorithm could generate lineages that have various levels of reproductive ability.

In Figure 7-figure supplement 2a, we summarized the overall scheme of analysis with single-cell tracking and cell-fate simulation. After the generation of live cell imaging videos, images were segmented and the segmented data was used for automatic single-cell tracking. To ensure the accuracy

of the tracking data, manual verification was performed, creating a cell-lineage database. Then, the database was used for cell-lineage map creation, data analysis, and generation of Operation data, which can also be saved. Operation data was then used for the cell fate simulation (Figure 7-figure supplement 2b). After loading the cell-lineage data, Operation data-Time and -Events were created. The length of time for progenitors and a primary event type were assigned to each progenitor, followed by the generation of cell-lineage data by assigning an event type and length of time to a cell. This process was repeated until the specified time. Example cell-lineage maps generated by empirical single-cell tracking analysis and the algorithm are shown in Figure 7-figure supplement 3a and b, respectively (cell-lineage maps generated by the algorithm have been deposited in Dryad). Furthermore, because the simulation *per se* can be carried out using Operation data, various simulation options can be created by modifying the Operation data content.

**Cell-fate simulation options with Operation data**

We created five different modes of simulations: Standard, Dose simulation, Mix culture, Sequential, and Mix culture-Sequential. The Standard mode simulates the fate of one cell type using one Operation data (Figure 8a). We applied this mode to simulate the expansion of a cell population for an extended period of time, which cannot be achieved by *in vitro* cell culture (Figures 9 and 11). The Dose simulation mode can be carried out using more than two sets of Operation data (Figure 8b) to obtain cellular responses to a treatment with a dose that has not been empirically examined. For example, if Operation data-Events A and B obtained from the single-cell analysis of cells treated with 2 and 5 μM of a drug, respectively, record the chances of bipolar cell division following a Start event of 10 and 1, respectively, the chance of a cell population exposed to 3 μM was calculated to be 7. The performance of such a calculation for each classified time and event data allows the generation of new (virtual) Operation data. We applied this mode to simulate cellular responses to different doses of MNNG

(Figure 10). For example, the fate of cells exposed to 5 μM MNNG can be simulated by creating Operation data for 5 μM MNNG from Operation data for 3 μM and 7 μM MNNG. The Mixed culture mode (Figure 8c) simulates a fate of a cell population composed of two or more types of cell populations using Operation data corresponding to each type of cell population. We applied this mode to simulate the expansion of cells under conditions in which 96% of cells were initially Control cells and 4% were p53 RNAi cells (Figure 12). The Sequential mode *per se* was not used in the current work, but this mode (Figure 8d) was used to perform virtual drug treatments. For example, simulation using the Operation data for Control cells was then switched to the second Operation data for cells treated with e.g. 3 μM MNNG, allowing simulation of the effect of 3 μM MNNG on Control cells. The Mixed culture with Sequential mode (Figure 8e) allowed simulations to be started with a virtual cell population composed of two or more different types of cell populations, with virtual drug treatment. Thus, if two types of cell population fates are to be simulated, two Operation data are used initially and then switched to Operation data for drug-treated cells of each type (Figure 13). If the cell types have different treatment sensitivities, the effects of this difference can be simulated by this mode. We applied this mode to simulate the impact of repeated MNNG treatments on the expansion of a cell population initially comprising 96% Control and 4% p53 RNAi cells at the start of the simulation (Figure 13h). In summary, cell-fate simulation using Operation data allows the creation of various simulation options and provides flexibility for designing virtual experiments that would be difficult to perform empirically.

**Number of progenitors used for simulation**

We characterized the algorithm by performing a series of test simulations. To distinguish data produced by simulation from one by single-cell tracking, we referred to the cells as, e.g. Control-Sim and MNNG7-Sim cells for the results produced by simulation (Figure 8-figure supplement 1). If the

corresponding Operation data needed to be indicated, the cell populations were referred to as, e.g. Operation data-Control and Operation data-MNNG7. We first performed simulations with 300, 500, 1,000, 1,500, and 2,000 progenitors with a simulation time of 15,000 min, repeated five times to detect variations in the simulation. Cell population expansion curves of virtually created Control cells (Control-Sim cells) are shown in Figure 8-figure supplement 1a. Under these conditions, the variation was < 2% of the average number of cells when the simulation was carried out with > 1,000 progenitors. The simulation performed using the Operation data-MNNG7 (Figure 8-figure supplement 1b) produced a larger variation, but this converged to about 6% when the simulation was carried out with > 1,000 progenitors. We therefore performed the simulation with 1,000–2,000 progenitors and repeated the simulation five to ten times (total of 5,000–10,000 progenitors).

**Comparison between cell population expansion curves determined by simulation and single-cell tracking**

We then evaluated the accuracy of the simulation by referencing the cell population expansion curves determined by single-cell tracking analysis (Figure 9). In the simulations, we used Standard mode with Operation data generated from the cell-lineage database, and performed simulation with 5,000 progenitors for 15,000 min. The number of progenitors was normalized to 100 to compare the results obtained by simulation with those obtained by single-cell tracking analysis. During the simulation, a Control-Sim cell population size increased 193.5-fold (5,000 to 967,281 cells), and about $2 \times 10^6$ virtual cells were created in the simulation period of 15,000 min. The Control-Sim, MNNG1-Sim, MNNG3-Sim, and MNNG7-Sim cell population expansion curves (Figure 9a, 0–4,000 min) were consistent with the curves determined using single-cell tracking analysis (Figure 2g), although the Control-Sim cell curve intersected with the MNNG1-Sim cell curve at a simulation time of about 10,000 min (Figure 9b, 0–15,000 min). To evaluate the accuracy of the simulation, we calculated the average percent difference between the cell numbers determined by the simulation and by single-cell

tracking analysis (Figure 9c-f). When the number of cells determined by single-cell tracking was calculated as 100%, the average difference was 1%–6%. We then performed a similar analysis with p53 RNAi cells and found that cell population expansion curves generated by the simulation showed consistent patterns (Figure 9g, 0–4,000 min, and Figure 9h, 0–15,000 min) with those determined by single-cell tracking analysis (Figure 2h). The percent differences were within 0–8% (Figure 9i-l). We thus concluded that the simulation could be performed within a variation of maximal 8% compared with the results of single-cell tracking analysis.

**Doubling time of cells generated by the simulation**

We also analyzed the doubling time of individual cells generated by single-cell tracking analysis and compared them with ones generated by simulation. The average cell doubling time was prolonged following the increased dose of MNNG (31.23 to 41.85 h, Figure 9-figure supplement 1a-d). The doubling time of individual cells generated by the simulation (Figure 9-figure supplement 1e-h) was similarly prolonged following the increase dose of MNNG (29.36 to 39.43 h), suggesting that the algorithm could simulate the effect of MNNG on cell doubling. Similarly, the effect of MNNG treatment on the cell doubling time of p53 RNAi cells (Figure 9-figure supplement 1i-l) could also be simulated (Figure 9-figure supplement 1m-p). On the other hand, the simulation tended to yield an average cell doubling time about 2 h shorter than that determined by single-cell tracking analysis. Given that the algorithm assigned a cell doubling time to each cell by generating a random number with Operation data-Time (Figure 7), a long cell doubling time, e.g. 3,000 min, which occurred less frequently, may be less likely to be assigned, resulting in the generation of a simulated cell population with a cell-doubling time about 2 h shorter than that of cells analyzed by single-cell tracking. This shorter average cell doubling time could translate into an increased rate of cell population expansion, and the maximal 8% variation in cell growth curves (Figure 9) could reflect the cell doubling time of the simulated cell population.

**Simulation of occurrence of multipolar cell division, cell death and cell fusion**

We examined how the algorithm simulated the occurrence of multipolar cell division, cell death, and cell fusion. Because these events were less frequent than bipolar cell division, simulations were performed 10 times with 1,000 progenitors (total 10,000 progenitors). We compared the numbers of these events generated within 4,000 min by the simulation with those obtained by single-cell tracking analysis. These data were then shown as the percent of total number of cells. The simulate results for multipolar cell division (Figure 9-figure supplement 2a), cell death (Figure 9-figure supplement 2b), and cell fusion (Figure 9-figure supplement 2c) show similar tendency with the single-cell tracking results, and the differences between the tracking analysis and simulate results were within 1%. We therefore concluded that the cell-fate simulation algorithm could perform virtual cell experiments with similar accuracy than single-cell tracking analysis.

**Virtual dose-response analysis and damage response**

To begin the study with the fate-simulation, we reanalyzed the responses of cells transfected with Scrambled siRNA or p53 siRNA to MNNG. To this end, Operation data were created for every 0.5 μM of MNNG from 0–7 μM using Dose simulation mode. The virtual dose-response curves determined by the simulation are shown in Figure 10a and b, and the numbers of cells at simulation times of 4,000 and 15,000 min (indicated by blue and red arrow, respectively, in Figure 10a and b) are shown as natural logarithm in Figure 10c and d, respectively. The dose-response curves of cells containing low levels of p53 (Control cells) and p53 RNAi cells determined at a simulation time of 4,000 min showed similar patterns to those determined by single-cell tracking (Figure 10c), suggesting that the fate of cells exposed to 0.5 μM increments of MNNG can be simulated by the Dose simulation mode. We then analyzed the effects of MNNG exposure on Control and p53 RNAi cells at 15,000 min, to determine the long-term impact of MNNG exposure. The cell population size of Control cells at 15,000 min was

reduced from 193,928 to 5,810 cells (Figure 10d, difference: 188,118 cells, 97%) by treatment with 7 μM MNNG, while the number of p53 RNAi cells was reduced from 113,075 to 12,055 cells (difference: 101,020 cells, 89%), suggesting that Control cells showed a stronger inhibitory response to MNNG than p53 RNAi cells, in terms of cell population expansion (Figure 10d). These results suggest that the sensitivity of p53 RNAi cells to MNNG was reduced by silencing the low levels of p53.

MNNG induces its cytotoxic effects through the formation of DNA breaks and activation of the response caused by the accumulation of p53 [26-32]. It is therefore conceivable that responses induced in Control cells may be related to both DNA-break formation and the response induced by the DNA damage-initiated accumulation of p53, while responses in p53 RNAi cells are only related to DNA-break formation. To estimate the relative contributions of these two effects to the inhibition of cell-population expansion, we plotted the population expansion curves of Control-Sim, MNNG7-Sim, p53 RNAi-Sim, and p53 RNAi-MNNG7-Sim cells and determined the population-doubling time (Figure 10e). We assumed that the difference in times between Control-Sim and MNNG7-Sim (7,150 min) was due to both effects, while the difference between p53 RNAi-Sim and p53 RNAi-MNNG7-Sim (4,510 min) represented the effect caused by the break formation. Based on these data, we estimated that about 63% and 37% of cell growth inhibition caused by 7μM MNNG exposure were due to effects related to DNA-break formation and the accumulation of p53, respectively. Although these percentages could be affected by other factors, dissecting the cellular response based on the possible mechanism of cytotoxicity could provide a deeper understanding of how cells respond to cytotoxic drugs.

**Survival of the progeny of multipolar cell division**

Next, we asked how frequently the progeny of multipolar cell division can survive and grow by performing a simulation in Standard mode with 2,500 progenitors for a simulation time of 20,000 min (13.8 days). Multipolar cell division-derived progeny, which lack reproductive ability (Figure 11a, left),

and progeny that underwent multipolar cell division followed by bipolar cell division, thereby maintaining reproductive ability (Figure 11a, right), are shown in burgundy and green, respectively. When the simulation was performed using the Operation data-Control (Figure 11b and c), no reproductive progeny produced by multipolar cell division were found. To visually show such cells, we created a computer animation (Figure 11-video 1 and Figure 11d for still image at 20,000 min), which visualizes the growth of the virtual cells, showing only burgundy cells that eventually underwent cell death or remained as non-growing cells. However, when the simulation was performed using Operation data-p53 RNAi (Figure 11e and f), some progeny of multipolar cell division underwent bipolar cell division, accounting for 0.72% of the cell population at a simulation time of 20,000 min. The computer animation (Figure 11-video 2 and Figure 11g for still image at 20,000 min) showed the expansion of green cells (cells survived and expand after multipolar cell division) in accordance with the suggestion [39, 40] that an aneuploid cell population could be generated by survival of the progeny of multipolar cell division, which was promoted by p53 silencing.

**Limiting expansion of p53 RNAi cells in the presence of Control cells**

We then investigated how the presence of Control cell influenced the growth of p53 RNAi cells, given that cells that lack p53 likely arise within a Control cell population during tumorigenesis. We performed a simulation based on the assumption that Control and p53 RNAi cells comprised 96% and 4% of the cell population, respectively, using Mixed culture mode with Operation data-Control and p53 RNAi. A total of $1.2 \times 10^7$ virtual cells were generated after 20,000 min of simulation, but the percentage of p53 RNAi cell population was reduced from 4% to 2.4% (Figure 12a) because of the frequent occurrence of multipolar cell division, cell death, and cell fusion (Figure 12b, and Figure 12-video 1 for the animation; p53 RNAi cells shown as blue cells). These data suggested that, although p53 RNAi cells could generate diversity in their cell population, the increased frequencies of multipolar cell division, cell death, and cell fusion compared with Control cells conferred a growth disadvantage

to p53 RNAi cells when both cell types co-existed in a cell population. We suggest that the occurrence of cell death in p53 RNAi cells may be the main factor limiting the expansion of these cells (Figure 5b). Indeed, a simulation using Operation data generated from p53 RNAi-Silico(-)cell death cells showed that the cells expanded at a similar rate to Control-Sim cells (Figure 12c), again suggesting that cell death acted as a major factor limiting the population size of p53 RNAi cells.

**Induction of damage response in Control cells and its impact on the expansion of p53 RNAi cell population**

The relative population-expansion rates of Control and p53 RNAi cells were altered by exposure to MNNG (Figure 10). We therefore simulated the responses of a cell population comprising Control (96%) and p53 RNAi cells (4%) to virtual MNNG treatment using the Mixed culture-Sequential mode. We used Operation data-Control and p53 RNAi up to a simulation time of 9,900 min, and the Operation data was then switched to the one for relevant doses of MNNG and the simulation was continued for another 10,000 min (total 20,000 min simulation) (Figure 13a). We simulated the responses of cells to 1.5, 3, 5, 6, and 7 μM MNNG. p53 RNAi cells were still unable to expand their population relative to Control cells following exposure to 1.5 and 3 μM MNNG (Figure 13b and c). However, p53 RNAi cells started to gain a growth advantage over Control cells after exposure to 5 μM MNNG (Figure 13d), and started to expand their population at doses of 6 and 7 μM MNNG (Figure 13e, f, and Figure 13-video 1). These results suggested that the damage responses induced in Control cells reduced its expansion speed while the expansion of the p53 RNAi cells continued (Figure 13g). Indeed, when the exposure of cells to 7 μM MNNG was repeated four times, 93% of the cell population was replaced with p53 RNAi cells (Figure 13h).

## DISCUSSION

Cell populations are known to be composed of cells with diverse phenotypic characteristics. Such diversity could be generated by the formation of a cell with distinct characteristics, and the subsequent expansion of its progeny in the cell population. In this study, we revealed that silencing of the low levels of p53 generated cells with distinct characteristics from Control cells, and also affected the responses of cells to MNNG. These results suggest that a novel approach using single-cell tracking and cell-fate simulation can provide unique insights into the function of p53, thus deepening our understanding of its role in tumorigenesis.

### Low levels of p53 and possible functions

p53 is required for cells to respond to stress, through regulation of its cellular content [4, 6, 7, 10-18]. The equilibrium between p53 degradation (through ubiquitination mediated by Mdm2) and its synthesis can be changed, depending on the degree of stress [4, 6, 7, 16-18]. Stronger stress tends to shift the equilibrium towards increased p53 levels, leading to various responses, e.g. metabolic regulation, DNA damage responses, autophagy, cell cycle regulation, and cell death [6, 10-15]. On the other hand, the functions of the low levels of p53 present in unstressed cells remain unclear, but they may have a housekeeping function. Indeed, several lines of evidence, including the promotion of induced pluripotent stem cells by silencing p53 [19], and the spontaneous formation of tetraploid cells, as proposed cancer precursor cells, in p53 knockout mice [10, 45], suggest that low levels of p53 are required for housekeeping and homeostasis functions in cells. In addition, Vousden and Lane pointed out that the low levels of p53 may play a role in responding to “daily levels of stress” [20], and Valente et al. recently demonstrated that p53 plays a role in responding to stress induced by physiological levels of oxygen tension [46]. Furthermore, the current study showed that low levels of p53 inhibited the induction of cell death and cell fusion, which could lead to the induction of multipolar cell division, suggesting that the low levels of p53 are involved in processes that ensure the accuracy of cell division.

**Silencing of low levels of p53 and induction of cell death, cell fusion, and multipolar cell division**

The different characteristics of Control and p53 RNAi cells are summarized in Figure 14a. Most Control cells underwent bipolar cell division, resulting in expansion of the cell population. Although cell death, cell fusion, and multipolar cell division occurred in Control cells, they had relatively little effect on the expansion of the cell population. In contrast, although p53 RNAi cells could expand their cell population through bipolar cell division, p53 silencing led to more frequent induction of cell death and cell fusion.

The cell death events in p53 RNAi cells appeared to be induced by a p53-independent mechanism. Although the mechanism underlying the induction of cell death remains to be investigated, it may involve a natural defense mechanism to remove cells lacking p53 from a cell population. Indeed, we demonstrated that cell death caused a 7.4% reduction in the rate of p53 RNAi cell population expansion. Cell death thus conferred a growth disadvantage to p53 RNAi cells relative to Control cells. Simulation of the fates of cells in a population containing 4% p53 RNAi and 96% Control cells showed that the proportion of p53 RNAi cells was reduced to 1.2% after 670 h of culture (Figure 14b). When such a simulation was initiated with 5,000 cells, the cell number reached ~$1 \times 10^9$, corresponding to ~1 cm of cancer tissue mass after 21 cell divisions. Within a cell tissue mass, p53 RNAi cells may occur as dormant cells, given that the percentage of p53 RNAi cells in the tissue would be reduced following the an increase in tissue size. With regard to dormancy, many metastatic cells are known to become dormant [47, 48], suggesting that their metastatic nature *per se* could confer a growth disadvantage on these cells relative to normal or non-metastatic cells, as indicated by the difference in expansion rates between p53 RNAi cells in a Control cell population.

Cell fusion was also increased following silencing of p53 (Figure 14a). Although the role of p53 in the suppression of cell fusion is unknown, previous reports have suggested a link between the loss of p53 and the induction of cell fusion. For example, fibroblasts derived from $p53^{-/-}$ mice rapidly became

tetraploid [10, 45]. Increased cell fusion of p53 RNAi cells, mainly between sibling cells produced by bipolar cell division, could account for the formation of tetraploid cells (Figure 14a). Such fused cells may be formed by failure of cytokinesis, mitotic slippage, or the formation of a link between siblings [43, 49-51]. However, low levels of p53 may block the process of fusion itself, given that we also observed cell fusion following abscission and between non-sibling cells. During development, e.g. myotube formation [52, 53], a cell fusion mechanism is activated, implying that cells can acquire a fusion-prone status. In addition to the physiological process of cell fusion, if cells, e.g. siblings produced by bipolar cell division, became fusion prone, it could lead to the formation of polyploid cells, which have been suggested to be precursors of cancer cells [49, 54-57]. The low levels of p53 may thus function to prevent cells from becoming fusion-prone, thereby reducing the risk of cells becoming cancer cells.

Loss of the low levels of p53 increased the induction of multipolar cell division following cell fusion (Figure 14a). The division of a cell into more than three cells generates progeny with different numbers of chromosomes. Although such aneuploid cells are generally fragile [39, 40], loss of p53 function has been suggested to contribute to the survival of aneuploid cells [58-60]. Indeed, we found that some such aneuploid cells underwent bipolar cell division and the progeny could propagate, creating an aneuploid cell population (Figure 14a). Even though gene mutation has been proposed as the main cause of cancer, aneuploidy is a near-universal feature of human cancers [61] and is also involved in the process of tumorigenesis [50]. Furthermore, impaired p53 function is known to cause frequent alterations in cell ploidy [49, 54-57]. The proposed process could thus be involved in the process of tumorigenesis. In summary, the low levels of p53 found in unstressed cells could suppress cell fusion, which leads to multipolar cell division, and loss of this function could thus create conditions favoring the generation of cancer cells.

**Response of p53-silenced cells to MNNG**

The above-mentioned context reveals the potential roles of low levels of p53 under unstressed conditions. One of the best-established roles of p53 is related to cellular responses induced following its accumulation under stressed conditions, including its capacity to prevent the survival of damaged cells. This capacity is closely associated with cell growth arrest and cell death. On the other hand, induction of the damage response in Control cells may oppose the suppression of tumor formation. Exposure of a cell population composed of 4% p53 RNAi cells and 96% Control cells to 7 μM MNNG, which could lead to the accumulation of p53, was associated with growth suppression of the Control cell population due to induction of the damage response, conferring an opportunity for expansion of the p53 RNAi cell population, which lacks the p53-mediated damage response function. Indeed, our simulation results suggested that 4% of p53 RNAi cells accounted for 93% of the cell population (containing 0.6% of aneuploid cells) after 40,000 min (27.78 days) if the population was exposed to 7 μM of MNNG every 10,000 min (Figure 14 c). These results suggest that exposure of tumor tissue composed of p53-proficient and -deficient cells to a reagent that induces a damage response may lead to preferential expansion of the p53-deficient cell population. If the deficient cells have a malignant nature, p53 could indirectly promote, rather than suppress the formation of a malignant tumor by suppressing the expansion of p53-proficient cell population. Understanding the role of p53 in tumorigenesis thus requires the delineation of its role at both the cellular and population levels. Furthermore, because most cancer cells carrying p53 gene mutations express mutated p53 in the cytoplasm instead of the nucleus, cytoplasmic mutated p53 has been suggested to confer a cellular function, referred to as gain-of-function [62-67]. Such cells may have a combined phenotype of both loss of wild type p53 and gain-of-function, or mutated p53 may alter the phenotype caused by the loss of the wild type p53. Nevertheless, these need to be considered in the context of p53-related tumorigenesis, and the current approach may be used to gain clues to reveal the context.

## Cell-fate simulation and its applications

Compared with other analytical methods, single-cell tracking analysis has the ability to accurately detect various cellular events, regardless of the frequency of their occurrence, by creating spatiotemporal data for individual cells. However, because single-cell tracking analysis is a morphological observation-based technique, we were unable to determine the silencing levels of p53 in individual cells. The availability of such information would allow deeper analysis, e.g. to examine the relationship between p53-silencing levels and the chance of cell fusion. Although it is difficult to monitor expression levels of p53, or other proteins or genes, in individual live cells using existing methods, new technologies combining single-cell tracking analysis with e.g. spatial transcriptomics [68, 69] could be developed to expand the applicability of this type of analysis. Such expansion could also provide additional flexibility for cell-fate simulations. We created a cell-fate simulation algorithm to allow the flexible design of various types of virtual experiments by creating Operation data, containing data generated by the categorization of event patterns. Such patterns could be further enriched by the addition of information on the expression levels of proteins or genes in individual cells, allowing the development of another new type of cell-fate simulation algorithm. Furthermore, given that each type of cell population tends to show a specific growth profile and response to treatment, the accumulation of public Operation data resources could be made accessible to various research projects to simulate the fate of cells of interest, predict the responses of cells to treatments, build models based on the simulations, and develop a theory-based model for cell behaviors. Because single-cell tracking data contains information on the motility of each cell, it may also be possible to simulate cell behaviors that could be influenced by cell-to-cell contact. This simulation-based biology could thus help to overcome some of the limitations associated with empirical cell biological studies, and provide greater flexibility in research with mammalian cells.

## Conclusions

p53 may affect cell population dynamics, and loss of 53 could lead to the formation of an aneuploid cell population. In addition, the dynamics of cell populations containing both p53-null cells and wild-type cells may be affected by the status of the wild-type cells. Our results suggest that wild-type cells could gain a growth advantage over p53-null cells in low-stress environments, while the growth balance between the p53-null and wild-type cells may change under stress conditions, allowing p53-null cells to gain a growth advantage. The role of p53 in the process of tumorigenesis may thus depend on the environment surrounding the cell population, as well as the p53 status of individual cells within the population. Revealing the status of individual cells by single-cell tracking and cell-fate simulation can thus further our understanding of the process of tumorigenesis.

## KEY RESOURCES TABLE

| Key Resources Table | | | | |
|---|---|---|---|---|
| **Reagent type (species) or resource** | **Designation** | **Source or reference** | **Identifiers** | **Additional information** |
| Antibody (mouse) | Mouse anti-p53 (DO-1, monoclonal) | Invitrogen | AHO0152 | 1 µg/mL |
| Antibody (goat) | Horseradish peroxidase conjugated goat anti-mouse antibody (polyclonal) | Abcam | Ab205719 | 1:25,000 |
| chemical compound, drug | *N*-methyl -*N′*-nitroso-*N*-nitrosoguanidine | Sigma-Aldrich | 129941 | |
| cell line (human) | A549-luc-C8 | Xenogen Corporation | N/A | |
| sequence-based reagent | p53 siRNA I | Cell Signaling Technology | 6231 | |
| sequence-based reagent | Control siRNA | Cell Signaling Technology | 6568 | |
| software, algorithm | MetaMorph (Quorum WaveFX, v7.8.12.0) | Quorum Technology | N/A | |
| software, algorithm | Image J. | Schneider et al., 2012 | https://imagej.nih.ggov/ij/ | |
| software, algorithm | Computerized single-cell lineage tracking analysis system software | Rancourt, Sato, and Satoh | BioRxiv. doi: https://doi.org/10.1101/508705. | |

| | | | | |
|---|---|---|---|---|
| software, algorithm | Cell fate simulation algorithm | This paper | | Results: Cell-fate simulation algorithm, Material and Methods: Overall flow of the cell-fate simulation algorithm, and Figure 7-Source code. |
| other | Cell lineage data | This paper | | Deposited in Dryad |

## MATERIALS AND METHODS

### Cells and cell culture

A549-luc-C8 cells were purchased from Xenogen Corporation and cultured in RPMI containing 10% fetal bovine serum (RPMI medium) in a humidified atmosphere with 5% $CO_2$. Cells were confirmed to be mycoplasma negative. Cells were plated in the center of each well of a cover glass Lab-Tek II 8-well chamber in 50 µL of cell suspension containing 3,500 cells and left to attach to the cover glass surface. Culture was continued for 24 h to allow more than 99% of cells attached to other cells, and culture medium (0.75 mL) was then added to each well and the chamber was viewed under a microscope (Olympus IX81) after 24 h of plating.

### Concurrent long-term live cell imaging, siRNA transfection, and MNNG treatment.

Concurrent long-term live cell imaging was performed as described previously [33, 36]. Briefly, images were acquired under a microscope using near infrared DIC imaging with a ×20 dry objective (UPlanSApo, 20×/0.75 NA, α/0.17/FN2G.5) and a ×1.5 coupler (Quorum Technologies) to generate a ×30-equivalent image. Images were acquired by area scanning (5 × 5 dimension, 512 × 512 pixels each, 1.77mm$^2$) using multi-dimensional acquisition mode in MetaMorph (Quorum Technology Inc., WaveFX, v7.8.12.0) with 34 ms exposure and XY piezo stage. Typically, 30 z-planes were acquired every 1 µm, and 512 × 512 pixel multi-layered .tiff files were created. Cells were maintained on the microscope stage in an environmental chamber (Live Cell Instrument, Korea) in a humidified atmosphere with 7.5% $CO_2$ and images were acquired every 10 min. Lipofection with scrambled siRNA and p53si RNA (Cell Signaling Technology) was performed approximately 24 h after cell plating using Effectene Transfection Reagent (Qiagen) with 1 µg siRNA in 742 µL transfection mixture, according to the supplier's instructions. Image acquisition was started immediately after siRNA transfection. At 24 h after siRNA treatment, cells were exposed to various doses of MNNG

(Sigma-Aldrich) for 30 min in serum-free RPMI, and the medium was then replaced with fresh RPMI medium. The evaporation rate of the medium was about 10 μl per 24 h, and each well of a cover glass Lab-Tek II 8-well chamber thus contained 800 μl of RPMI medium to minimize the impact of evaporation on cell growth. The RPMI medium contained phenol red to monitor the pH of the medium, and 7.5% $CO_2$ was typically required to maintain an optimal pH

Image files corresponding to each field of view were saved using MetaMorph on the hard drive of a Windows computer. The files were then transferred automatically to a Macintosh computer (OS15) using in-house software [33]. Unique file names were assigned to each file for archiving, followed by the creation of an all-in-focus image using in-house software [33]. The focused images were positioned and the contrast was adjusted to create stitched images (25 images covering 5 × 5 dimension, approximately 2500 × 2500 pixels). The images were then saved in chronological order for display. File transferring, focused image creation, image positioning, and contrast adjustment were performed automatically, and eight stitched images that corresponding to each Lab-Tek II 8-well chamber well were typically created concurrently in an automatic manner [33]. The files were displayed using an in-house movie player, to monitor the progress of live-cell imaging [33].

**DIC image segmentation**

Image segmentation was performed using our image segmentation software (for details see [33]). Image segmentation can be performed by various methods, e.g. region growing by setting an optimal parameter for an image. However, the optimal parameter for a time point of the image may be difficult to use for other time points, given that the optimal parameter is affected by the cell density and size, the relative location of a cell to other cells, the formation of cell debris, and image-quality variations caused by the microscope system. We typically processed > 8,000 images, and our segmentation software was therefore developed to perform DIC image segmentation automatically, regardless of

image quality [33]. Briefly, in a DIC image, cells appear as illuminated objects associated with a shadow, and this rule can be applied to any cells in an image. For example, if a flat cell is located behind a bulky cell, the flat cell appears as a darker cell, but the cell itself is brighter than its shadow. Our segmentation software used these characteristics of the DIC images. The mean pixel value of a DIC image (256 grayscale images) was first adjusted to a grayscale value of 100, and four images were then created by applying four different pixel threshold values: e.g. > 200, > 180, > 160, and > 150. The image with the highest threshold value was used first, and connected pixels, representing an area, were identified by connectivity analysis. The connected pixels were then overlaid on an original DIC image and the area of connected pixels was extended. The connected pixels were likely to represent the illuminated cells in the image, and expansion was carried out to identify the possible borders of the cells. The connected areas were then overlaid on the image created with the second highest grayscale threshold value. Connectivity analysis was performed, except for the areas where a connected area had already been set in the previous step. This process allowed us to identify darker cells in a DIC image than those identified previously. Connected areas identified in the second step were overlaid on the original DIC image and the area was expanded to find a border of darker cells. The same process was repeated for the images created by the third and fourth thresholds to identify cells in an image. By this approach, DIC images of various qualities could be segmented.

**Single-cell tracking**

Single-cell tracking analysis was performed using in-house software that tracked cells automatically, detected cellular events, and allowed verification of the tracking results [33]. Single-cell tracking was started by selecting a connected area (Area 1) that corresponded to a progenitor. Because the segmentation pattern of the next image was often changed, automatic cell tracking was performed by identifying the best-matched segmented area in the next image. Briefly, Area 1 was overlaid on the connected areas in the next time-point image. If Area 1 overlapped with one area in the next image and

the size of the area was within the 2-fold of Area 1, the area in the next image was determined as the area that corresponded to the cell that was being tracked. If Area 1 overlapped with one area in the next image, but the size of the area was larger than twice Area 1, the area was likely divided into multiple areas and one area that overlapped with Area 1 was determined as the area corresponding to the tracked cell. If multiple areas in the next image overlapped with Area 1, the multiple areas were likely merged and the merged area was determined as the area corresponding to the tracked cell. This process was carried out for all selected progenitors and repeated until the predetermined time point. When the tracking reached the target time point, manual data verification was performed to correct tracking errors. Detected errors were corrected manually, and automatic single-cell tracking was restarted. Typically, verification was performed every 100 time points to create error-free cell-lineage data. The required time for verification was ~48 h for the tracking of 400 Control progenitors and their progeny for 400 time points. Concerning event detection, different approaches were used for cell division, cell fusion, and cell death. Bipolar and multipolar cell division were detected by first identifying a mitotic round cell. Typically, such cells appeared as bright round objects in DIC images. The in-house cell-tracking software thus built a data library of the shapes of mitotic cells, and determined if a tracked cell underwent mitosis. During the manual verification step, if an error, e.g. detection of a non-mitotic cell as a mitotic one or failure to detect a mitotic cell, was found, the failed or missed pattern was incorporated into the software to improve the subsequent detection accuracy. Following the detection of mitotic cells, if a connected area overlapped with two, three, and four connected areas in the next image, the software determined that bipolar, tripolar, and tetrapolar cell division, respectively, had occurred. Concerning cell fusion, if two connected areas corresponding to two different cells overlapped with the same connected area in the next image, and the area did not divide into multiple areas in the next 10–20-time points, the software determined that two cells were fused. In the case of cell death, dead cells typically formed remnants that appeared as bright, irregularly shaped objects. If a

connected area overlapped with an area corresponding to such an object, and the object was also found in the next 10–20 time-point images, the software determined that cell death had occurred.

Automated cell tracking and manual verification can be used to generate an error-free cell-lineage database. Furthermore, to ensure complete cell-lineage data, if any progeny of a cell lineage moved outside of the field of view, all the data corresponding to that lineage were excluded from the analyses. During single-cell tracking, information on cell-lineage number, cell number, the coordinates of the cells, the types of an events occurring in the cell, the relationship of a cell to its parent cell, and information related to fused cells were recorded in the cell-lineage database[33].

**Western blotting**

Cells were transfected with scrambled siRNA and p53 siRNA and treated with various doses of MNNG after 24 h. At 48 h after treatment, the cells were harvested and proteins (15 µg) were separated by 10% sodium dodecyl sulfate-polyacrylamide gel electrophoresis. Western blotting was performed using anti-p53 antibody (1 µg/mL, DO-1; Invitrogen) and horseradish peroxidase-conjugated goat anti-mouse antibody (25,000-fold dilution; Abcam). Proteins were visualized using an ECL reagent (Pierce). Quantitation of p53 was performed using Image J.

**Generation of density maps**

To create a cell density map, we assigned a value of one to a pixel within the 20-pixel diameter area for cell density and 100-pixel diameter area for multipolar cell division and cell death density from the position of the cell or position where multipolar cell division or cell death occurred. If an area overlapped with other areas, a pixel was assigned the sum of the number of overlapped areas. These values were used to generate heat maps.

**Overall flow of the cell-fate simulation algorithm**

The flow of the cell-fate simulation algorithm is shown in Figure 7-figure supplement 1a. The simulation mode was selected from the available five modes; Standard, Dose simulation, Mix culture, Sequential, and Mix culture-Sequential (Figure 7-figure supplement 1a, 1 and Figure 8). Standard mode performed a simulation by setting a simulation time (Sim. Time end) and an initial number of cells (Init. No. of cells; progenitors) followed by Operation data creation (Figure 7-figure supplement 1a, 2, and Figure 7-figure supplement 1b) or uploading, and generation of simulation arrays (Figure 7-figure supplement 1a, 3, and Figure 7-figure supplement 1b). Operation data held the categorized information of events, and Simulation arrays (Figure 7-figure supplement 1a, 3) were used to assign the length of time between two events (LT) and event type. Dose response mode was carried out by setting a simulation time, the initial number of cells, and an intermediate dose. Two sets of Operation data were then generated or uploaded and virtual Operation data corresponding to the intermediate dose were created using those Operation data. For example, if the intermediate dose was 5 μM MNNG, virtual Operation data were generated from Operation data for 3 μM and 7 μM MNNG. Mixed culture mode performed a simulation for a virtual cell population composed of two cell types. A simulation time and initial numbers of the first and second cell populations were set. Two sets of Operation data were used to simulate the growth of the first and second cell populations individually. Two sets of simulation arrays were also created. This mode could be used to simulate the growth of a cell population surrounded by another cell population. Sequential mode was used to perform virtual drug treatment. The simulation times before and after treatment, and the initial number of cells were set. Two sets of Operation data for the first and second doses were used, and simulation arrays corresponding to each dose were created. Mixed culture-Sequential mode was a combined version of Mixed culture and Sequential. This mode used four sets of Operation data and generated four sets of simulation arrays. Initial processing was then performed by creating a cell data information array (CDI) that included the LT and event type assigned to each cell (Figure 7-figure supplement 1a, 4, and Figure 7-figure supplement 1d). Based on the information in the CDI, a virtual cell-lineage database was created

(Figure 7-figure supplement 1a, 5, and Figure 7-figure supplement 1e). After these initial processes, a repeated cycle of assigning LT and event type (Figure 7-figure supplement 1f), reassigning LT and event type to adjust for the effect of cell fusion on LT (Figure 7-figure supplement 1g), and creating a virtual cell-lineage database (Figure 7-figure supplement 1h) were carried out until the simulation time was reached (Figure 7-figure supplement 1a, 6). If Sequential or Mixed culture-Sequential mode was used, the cell-lineage database end was trimmed (Figure 7-figure supplement 1i), Operation data was switched to corresponding Operation data, and the process proceeded to the second round of the repeated cycle (Figure 7-figure supplement 1a, 7). When processing reached the simulation time, the simulation was terminated and the results were displayed.

**Cell-fate simulation algorithm: Operation data**

Processing related to Operation data, which comprised three types of data, is outlined in Figure 7-figure supplement 1b. Operation data were either uploaded or generated from a cell-lineage database. If the Operation data were generated, information held in the cell-lineage database was converted into an Operation data-Time (Figure 7-figure supplement 1b, 1), Operation data-Event (Figure 7-figure supplement 1b, 2), and Recovery data (Figure 7-figure supplement 1b, 3). The Operation data-Time held categorized LT by event type, e.g. LT between bipolar cell division and cell death (BD-CD data type) and LT from time 0 min to the time that an event occurred in a progenitor (First event data type) (Figure 7-figure supplement 1b, 1). The Operation data-Event contained the frequency of events occurred following, e.g. bipolar cell division (BD data type), or multipolar cell division (MD data type) (Figure 7-figure supplement 1b, 2). Recovery data was used to simulate the rate of recovery a cell population from the treatment of MNNG. When cells were treated with MNNG, the majority of cells may be killed. However, small number of cells gained reproductive ability, which could be found at the end of imaging. Thus, the Recovery was the percentage of cell lineages that underwent cell division at the end of single-cell tracking (Figure 7-figure supplement 1b, 3). For example, if any of the progeny

derived from a progenitor underwent bipolar cell division at last within 20% of the single-cell tracking period, e.g. 320 to 400 min when tracking was performed for 400 min, this cell lineage was counted as one upon the calculation of the percentage. Thus, if 10 such cell lineages were found out of a total of 300, the recovery percent was 3.3%. Using Dose response mode, virtual Operation data were created from two sets of Operation data using the formula: virtual Operation data = Operation data 1 + [(Operation data 2 − Operation data 1)/(Dose 2 −Dose 1)]×(Intermediate dose − Dose 1) (Figure 7-figure supplement 1b, 4).

**Cell-fate simulation algorithm: Simulation arrays**

The dataset stored in Operation data was then converted into Simulation arrays that were used to assign LT and event types (Figure 7-figure supplement 1c). In the Operation data, each categorized Operation data-Time was stored in the format, i.e. LT, and the number of LT that was found. For example, 20 min of LT found four times was written as 20:4. In the Simulation arrays corresponding to the Operation data-Time, this was converted to, e.g. 20, 20, 20, 20. If no corresponding type of event occurred, the array for the event held no data. To generate a simulation array for the Operation data-Event, the percentage of each event relative to the total number of cell divisions (total of bipolar cell division and multipolar cell division) was calculated. The maximum number of entries per array was 100. The total percentage of events could thus exceed 100, e.g. first event list (bipolar cell division, cell death, multipolar cell division, and the number of cells with no cell division (nonDiv)). In this case, the percentage of each event was adjusted to make a total of 100. If the percentage of the event was < 100, 0 was filled to make the total entry for the array 100. If no corresponding type of event occurred, an array for the event held no data. The Recovery percentage was calculated as described above.

**Cell-fate simulation algorithm: Initial LT and event-type assignment.**

In the first event assignment (Figure 7-figure supplement 1d), the CDI that held the status of each cell throughout a simulation was created. In this step, the cell-lineage number was generated following the initial number of cells set previously, and the cell number 0 was assigned to each progenitor. Using the FirstEvent array, LT was then assigned to each cell. If the array was empty, the average time that bipolar cell division occurred was calculated and −25% to +25% of the time selected by random number was assigned as LT, and bipolar cell division was then assigned to the cell. If the FirstEvent array held data, LT was assigned by creating a random number, but if LT was equal to the length of single-cell tracking, −30% to +30% of the length of the time of single-cell tracking was assigned as LT and the event type was selected using the FirstEvent list array. If there was no entry in the array, NonDiv was assigned, otherwise, bipolar cell division, multipolar cell division, or cell death was assigned. If cell death was assigned, LT was reassigned using the NonDivCD time data array.

**Cell-fate simulation algorithm: Initial cell-lineage database creation**

The cell-lineage database was created using information held by the CDI (Figure 7-figure supplement 1e). This array contained information regarding LT and event type as a blueprint of the virtual cells (Figure 7-figure supplement 1e). If LT exceeded the simulation time set previously, LT was adjusted to a time equal to the simulation time, otherwise, a cell-lineage database was generated composed of an X position, Y position, time point, event type, cell-lineage number, cell number, parent cell information, cell number and the cell-lineage number of the cell that was fused in the event of cell fusion. If the event type was bipolar cell division or multipolar cell division, information related to the progeny created by bipolar cell division or multipolar cell division was entered into the CDI following the generation of corresponding cell numbers for each progeny.

**Cell-fate simulation algorithm: LT and event-type assignment**

In the repeated assignment cycle (Figure 7-figure supplement 1a, 6), the next LT and event type was determined based on the current event type. If the current event in a cell was NonDiv (Figure 7-figure supplement 1f, 1), a randomized number between 0 and 100 was generated, and if the number was lower than the Recovery %, bipolar cell division was assigned to the cell. In the next cycle, this cell was entered into a growing cycle. If the LT was 80%–100% of the length of the single-cell tracking time, the LT was determined by generating random numbers between 80 and 100. Assignment of bipolar cell division in this manner only occurred once at the first cycle of the assignment. If the random value was higher than the Recovery %, either NonDiv or cell death was assigned, in which case the % of cell death of total cell division was calculated and, if the random number between 0 and 100 was lower than the cell death %, a cell death was assigned. In this case, LT was assigned using the NonDivCD time array. If the random number between 0 and 100 was higher than the cell death %, NonDiv was assigned, and the length of single-cell tracking time was assigned as LT.

Next, if the current event was bipolar cell division, information related to its sibling was searched for. If a sibling was found, either bipolar cell division, multipolar cell division, or cell death was assigned using the Bipolar cell division list array, otherwise bipolar cell division, multipolar cell division, cell fusion, or cell death was assigned. If the event assigned by the Bipolar cell division list array was cell fusion, then its sibling was again searched. If no sibling was found, LT was assigned by the BDCF time array. If the array was empty, the event type was changed to cell death and the average time that cell death occurred was set as LT. If a sibling was found, LT was assigned using the BDCF time array. If the array was empty, cell fusion was changed to cell death and the average cell death time was set as LT. If LT was set, but it was longer than the LT of its sibling, LT was made shorter than the sibling's LT. If the event assigned using the Bipolar cell division list array was bipolar cell division, LT was assigned by the BDBD time array. If the array was empty, the average bipolar cell division time was set as LT. If LT was set by the BDBD time array but the LT was not within −10% to +10% of LT of its parent cell, LT was reselected until the LT fell within this range. If LT assigned by the Bipolar

cell division list array was multipolar division, LT was assigned by the BDBD time array. If the array was empty, the average bipolar cell division time was set as LT. If the event assigned by the Bipolar cell division list array was cell death, LT was assigned the BDCD time array. If the array was empty, the average cell death time was set as LT.

If the current event was multipolar cell division, information related to its siblings was searched for. If siblings were found and cell fusion was assigned to two siblings, either bipolar cell division, multipolar cell division, or cell death was assigned by the Multipolar cell division list array, otherwise bipolar cell division, multipolar cell division, cell fusion, or cell death was assigned. If the event assigned by the Multipolar cell division list array was cell fusion, then, event type of its sibling was again searched. If no sibling was found, LT was assigned by the MDCF time array. If the array was empty, the event type was changed to cell death, and the average time that cell death occurred was set as LT. If only one sibling was found, LT was assigned by the MDCF time array. If the array was empty, cell fusion was changed to cell death and the average cell death time was set as LT. If two siblings were found and cell fusion was assigned to one of the siblings, LT was assigned by the MDCF time array. If the array was empty, cell fusion was changed to cell death and the average cell death time was set as LT. If LT was longer than the LT of its siblings, LT was made shorter than its siblings. If cell fusion was not assigned to any of its siblings, LT was assigned by the MDCF time array. If the array was empty, cell fusion was changed to cell death and the average cell death time was set as LT. If the event assigned by the Multipolar cell division list array was bipolar cell division, LT was assigned by the MDMD time array. If the array was empty, the average bipolar cell division time was set as LT. If LT assigned by the Multipolar cell division list array was multipolar cell division, LT was assigned by the MDMD time array. If the array was empty, the average bipolar cell division time was set as LT. If the event assigned by the Multipolar cell division list array was cell death, LT was assigned by the MDCD time array. If the array was empty, the average cell death time was set as LT.

**Cell-fate simulation algorithm: Readjustment of LT in cells that underwent cell fusion**

If cell fusion occurred in a cell, the LT of the cell being fused was often affected and the LT was readjusted (Figure 7-figure supplement 1g). If the current event was bipolar cell division, the next event was assigned by the BDCF lists. If the next event was bipolar cell division or multipolar cell division, LT was assigned by the DivCFDiv time array, and if the next event was cell death, LT was assigned by the BDCFCD array. If the current event was multipolar cell division, the next event was assigned by the MDCF lists. If the next event was bipolar cell division or multipolar cell division, LT was assigned by the DivCFDiv time array, and if the next event was cell death, LT was assigned by the MDCFCD array.

**Cell-fate simulation algorithm: Cell-lineage database creation**

The cell-lineage database was created using information held by the CDI (Figure 7-figure supplement 1h). If LT exceeded the simulation time set previously, LT was adjusted to a time equal to the simulation time. If the event type was bipolar cell division or multipolar cell division, information related to the progeny created by bipolar cell division or multipolar cell division was entered into the CDI following the generation of corresponding cell numbers for each progeny. If the event type was cell fusion, cells to be fused were searched and relevant information regarding cell-lineage number and cell number was recorded for the cell.

**Cell-fate simulation algorithm: Trimming the end of the cell-lineage database**

In Sequential and Mixed culture-Sequential modes, the end of the cell-lineage data was trimmed to the nearest cell division event (Figure 7-figure supplement 1i) before entering the second repeated cycle of assignment.

**Statistical analysis**

Statistical analyses were performed by Prism 8.

**Naming rule for cells and Operation data**

A549 cells treated with scrambled siRNA and p53 siRNA are referred to as Control and p53 RNAi cells, respectively. Those cells treated with MNNG are named by adding, e.g. Control-MNNG1 (cells treated with 1 μM of MNNG). If a cell population that is generated by cell fate simulation is referred, -Sim was added, e.g. Control-Sim and Control-MNNG1-Sim. In the case that cells generated in silico to remove cell death are referred, cells are named e.g. Control-Silico(-)cell death. If an Operation data-Time or Operation data-Events are required to be specified, the name of cells was added following Operation data, e.g. Operation data-Control.

**ACKNOWLEDGEMENTS**

We thank Amélie Fradet-Turcotte for critical reading of the manuscript. We like to acknowledge the Bioimaging Platform of Research Centre for Infectious Diseases for the technical support of microscopes. This work was supported by the Canadian Foundation for Innovation and Canadian Institutes for Health Research.

**DECLARATION OF INTERESTS**

The authors declare no competing interests.

**DATA AVAILABILITY**

All data generated or analyzed during this study are included in the paper and supporting file; Source Data files have been provided for Figure 1-figure supplements 2-4, Figures 2, Figures 3, Figures 4, Figure 4-figure supplement 1, Figures 5, Figures 6, Figure 7-figure supplements 1-3, Figure 8-figure

supplement 1, Figure 9, Figure 9-figure supplement 1 and 2, and Figures 10-13. Source code has been provided for Figure 7.

Figure 1-videos (cellular events), Figure 2-figure supplements (cell-lineage maps), Figure 2-videos (single-cell tracking), Figure 2-source data (cell-lineage database), and Figure 7-figure supplement (cell-lineage maps) have been deposited in Dryad.

## REFERENCES


1. Kandoth, C. et al. Mutational landscape and significance across 12 major cancer types. *Nature* **502**, 333-339 (2013).
2. Hollstein, M., Sidransky, D., Vogelstein, B. & Harris, C.C. p53 mutations in human cancers. *Science* **253**, 49-53 (1991).
3. Petitjean, A. et al. Impact of mutant p53 functional properties on TP53 mutation patterns and tumor phenotype: lessons from recent developments in the IARC TP53 database. *Hum Mutat* **28**, 622-629 (2007).
4. Boutelle, A.M. & Attardi, L.D. p53 and Tumor Suppression: It Takes a Network. *Trends Cell Biol* **31**, 298-310 (2021).
5. Levine, A.J. The many faces of p53: something for everyone. *J Mol Cell Biol* **11**, 524-530 (2019).
6. Kastenhuber, E.R. & Lowe, S.W. Putting p53 in Context. *Cell* **170**, 1062-1078 (2017).
7. Lavin, M.F. & Gueven, N. The complexity of p53 stabilization and activation. *Cell Death Differ* **13**, 941-950 (2006).
8. Vogelstein, B., Lane, D. & Levine, A.J. Surfing the p53 network. *Nature* **408**, 307-310 (2000).
9. Hafner, A., Bulyk, M.L., Jambhekar, A. & Lahav, G. The multiple mechanisms that regulate p53 activity and cell fate. *Nat Rev Mol Cell Biol* **20**, 199-210 (2019).
10. Livingstone, L.R. et al. Altered cell cycle arrest and gene amplification potential accompany loss of wild-type p53. *Cell* **70**, 923-935 (1992).
11. Kastan, M.B. et al. Levels of p53 protein increase with maturation in human hematopoietic cells. *Cancer Res* **51**, 4279-4286 (1991).
12. Clarke, A.R. et al. Thymocyte apoptosis induced by p53-dependent and independent pathways. *Nature* **362**, 849-852 (1993).

13. Lowe, S.W., Schmitt, E.M., Smith, S.W., Osborne, B.A. & Jacks, T. p53 is required for radiation-induced apoptosis in mouse thymocytes. *Nature* **362**, 847-849 (1993).

14. Campisi, J. Senescent cells, tumor suppression, and organismal aging: good citizens, bad neighbors. *Cell* **120**, 513-522 (2005).

15. Rufini, A., Tucci, P., Celardo, I. & Melino, G. Senescence and aging: the critical roles of p53. *Oncogene* **32**, 5129-5143 (2013).

16. Haupt, Y., Maya, R., Kazaz, A. & Oren, M. Mdm2 promotes the rapid degradation of p53. *Nature* **387**, 296-299 (1997).

17. Honda, R., Tanaka, H. & Yasuda, H. Oncoprotein MDM2 is a ubiquitin ligase E3 for tumor suppressor p53. *FEBS Lett* **420**, 25-27 (1997).

18. Kubbutat, M.H., Jones, S.N. & Vousden, K.H. Regulation of p53 stability by Mdm2. *Nature* **387**, 299-303 (1997).

19. Guo, S. et al. Nonstochastic reprogramming from a privileged somatic cell state. *Cell* **156**, 649-662 (2014).

20. Vousden, K.H. & Lane, D.P. p53 in health and disease. *Nat Rev Mol Cell Biol* **8**, 275-283 (2007).

21. Kruiswijk, F., Labuschagne, C.F. & Vousden, K.H. p53 in survival, death and metabolic health: a lifeguard with a licence to kill. *Nat Rev Mol Cell Biol* **16**, 393-405 (2015).

22. Lassus, P., Ferlin, M., Piette, J. & Hibner, U. Anti-apoptotic activity of low levels of wild-type p53. *EMBO J* **15**, 4566-4573 (1996).

23. Chow, K.K. et al. Imaging cell lineage with a synthetic digital recording system. *Science* **372** (2021).

24. Chapal-Ilani, N. et al. Comparing algorithms that reconstruct cell lineage trees utilizing information on microsatellite mutations. *PLoS Comput Biol* **9**, e1003297 (2013).

25. Zafar, H., Lin, C. & Bar-Joseph, Z. Single-cell lineage tracing by integrating CRISPR-Cas9 mutations with transcriptomic data. *Nat Commun* **11**, 3055 (2020).

26. Lindahl, T., Sedgwick, B., Sekiguchi, M. & Nakabeppu, Y. Regulation and expression of the adaptive response to alkylating agents. *Annu Rev Biochem* **57**, 133-157 (1988).

27. Kim, W.J., Beardsley, D.I., Adamson, A.W. & Brown, K.D. The monofunctional alkylating agent N-methyl-N'-nitro-N-nitrosoguanidine triggers apoptosis through p53-dependent and -independent pathways. *Toxicol Appl Pharmacol* **202**, 84-98 (2005).

28. Wood, R.D. DNA repair in eukaryotes. *Annu Rev Biochem* **65**, 135-167 (1996).

29. Jacobs, A.L. & Schar, P. DNA glycosylases: in DNA repair and beyond. *Chromosoma* **121**, 1-20 (2012).

30. Lindahl, T. Repair of intrinsic DNA lesions. *Mutat Res* **238**, 305-311 (1990).

31. Satoh, M.S. & Lindahl, T. Role of poly(ADP-ribose) formation in DNA repair. *Nature* **356**, 356-358 (1992).

32. Lindahl, T., Satoh, M.S., Poirier, G.G. & Klungland, A. Post-translational modification of poly(ADP-ribose) polymerase induced by DNA strand breaks. *Trends Biochem Sci* **20**, 405-411 (1995).

33. Sato, S., Rancourt, A. & Satoh, M.S. Identification of SNA-I-positive cells as stem-like cells in an established cell line using computerized single-cell lineage tracking. *BioRxiv* **508705; doi:** https://doi.org/10.1101/508705 (2018).

34. Puck, T.T., Marcus, P.I. & Cieciura, S.J. Clonal growth of mammalian cells in vitro; growth characteristics of colonies from single HeLa cells with and without a feeder layer. *J Exp Med* **103**, 273-283 (1956).

35. Ganem, N.J., Godinho, S.A. & Pellman, D. A mechanism linking extra centrosomes to chromosomal instability. *Nature* **460**, 278-282 (2009).

36. Sato, S., Rancourt, A., Sato, Y. & Satoh, M.S. Single-cell lineage tracking analysis reveals that an established cell line comprises putative cancer stem cells and their heterogeneous progeny. *Sci Rep* **6**, 23328 (2016).

37. Boveri, T. Concerning the origin of malignant tumours by Theodor Boveri. Translated and annotated by Henry Harris. *J Cell Sci* **121 Suppl 1**, 1-84 (2008).

38. Keryer, G., Ris, H. & Borisy, G.G. Centriole distribution during tripolar mitosis in Chinese hamster ovary cells. *J Cell Biol* **98**, 2222-2229 (1984).

39. Holland, A.J. & Cleveland, D.W. Boveri revisited: chromosomal instability, aneuploidy and tumorigenesis. *Nat Rev Mol Cell Biol* **10**, 478-487 (2009).

40. Gisselsson, D. et al. When the genome plays dice: circumvention of the spindle assembly checkpoint and near-random chromosome segregation in multipolar cancer cell mitoses. *PLoS One* **3**, e1871 (2008).

41. Saunders, W. Centrosomal amplification and spindle multipolarity in cancer cells. *Semin Cancer Biol* **15**, 25-32 (2005).

42. Emdad, L., Sarkar, D., Su, Z.Z. & Fisher, P.B. Emerging roles of centrosomal amplification and genomic instability in cancer. *Front Biosci* **10**, 728-742 (2005).

43. Shi, Q. & King, R.W. Chromosome nondisjunction yields tetraploid rather than aneuploid cells in human cell lines. *Nature* **437**, 1038-1042 (2005).

44. Rajagopalan, H. & Lengauer, C. Aneuploidy and cancer. *Nature* **432**, 338-341 (2004).

45. Harvey, M. et al. In vitro growth characteristics of embryo fibroblasts isolated from p53-deficient mice. *Oncogene* **8**, 2457-2467 (1993).

46. Valente, L.J. et al. p53 deficiency triggers dysregulation of diverse cellular processes in physiological oxygen. *J Cell Biol* **219** (2020).

47. Husemann, Y. et al. Systemic spread is an early step in breast cancer. *Cancer Cell* **13**, 58-68 (2008).

48. Riethmuller, G. & Klein, C.A. Early cancer cell dissemination and late metastatic relapse: clinical reflections and biological approaches to the dormancy problem in patients. *Semin Cancer Biol* **11**, 307-311 (2001).

49. Eischen, C.M. Genome Stability Requires p53. *Cold Spring Harb Perspect Med* **6** (2016).

50. Ganem, N.J., Storchova, Z. & Pellman, D. Tetraploidy, aneuploidy and cancer. *Curr Opin Genet Dev* **17**, 157-162 (2007).

51. Storchova, Z. & Kuffer, C. The consequences of tetraploidy and aneuploidy. *J Cell Sci* **121**, 3859-3866 (2008).

52. Hernandez, J.M. & Podbilewicz, B. The hallmarks of cell-cell fusion. *Development* **144**, 4481-4495 (2017).

53. Shinn-Thomas, J.H. & Mohler, W.A. New insights into the mechanisms and roles of cell-cell fusion. *Int Rev Cell Mol Biol* **289**, 149-209 (2011).

54. Deangelis, P. et al. P53 expression is associated with a high-degree of tumor DNA aneuploidy and incidence of p53 gene mutation, and is localized to the aneuploid component in colorectal carcinomas. *Int J Oncol* **3**, 305-312 (1993).

55. Dutertre, S., Hamard-Peron, E., Cremet, J.Y., Thomas, Y. & Prigent, C. The absence of p53 aggravates polyploidy and centrosome number abnormality induced by Aurora-C overexpression. *Cell Cycle* **4**, 1783-1787 (2005).

56. Galipeau, P.C. et al. 17p (p53) allelic losses, 4N (G2/tetraploid) populations, and progression to aneuploidy in Barrett's esophagus. *Proc Natl Acad Sci U S A* **93**, 7081-7084 (1996).

57. Ramel, S. et al. Inactivation of p53 and the development of tetraploidy in the elastase-SV40 T antigen transgenic mouse pancreas. *Pancreas* **11**, 213-222 (1995).

58. Fujiwara, T. et al. Cytokinesis failure generating tetraploids promotes tumorigenesis in p53-null cells. *Nature* **437**, 1043-1047 (2005).

59. Thompson, S.L. & Compton, D.A. Examining the link between chromosomal instability and aneuploidy in human cells. *J Cell Biol* **180**, 665-672 (2008).

60. Vitale, I. et al. Multipolar mitosis of tetraploid cells: inhibition by p53 and dependency on Mos. *EMBO J* **29**, 1272-1284 (2010).

61. Li, R. & Zhu, J. Effects of aneuploidy on cell behaviour and function. *Nat Rev Mol Cell Biol* (2022).

62. Acin, S. et al. Gain-of-function mutant p53 but not p53 deletion promotes head and neck cancer progression in response to oncogenic K-ras. *J Pathol* **225**, 479-489 (2011).

63. Amelio, I. & Melino, G. Context is everything: extrinsic signalling and gain-of-function p53 mutants. *Cell Death Discov* **6**, 16 (2020).

64. Bargonetti, J. & Prives, C. Gain-of-function mutant p53: history and speculation. *J Mol Cell Biol* **11**, 605-609 (2019).

65. Oren, M. & Rotter, V. Mutant p53 gain-of-function in cancer. *Cold Spring Harb Perspect Biol* **2**, a001107 (2010).

66. van Oijen, M.G. & Slootweg, P.J. Gain-of-function mutations in the tumor suppressor gene p53. *Clin Cancer Res* **6**, 2138-2145 (2000).

67. Yue, X. et al. Mutant p53 in Cancer: Accumulation, Gain-of-Function, and Therapy. *J Mol Biol* **429**, 1595-1606 (2017).

68. Hou, X. et al. Integrating Spatial Transcriptomics and Single-Cell RNA-seq Reveals the Gene Expression Profling of the Human Embryonic Liver. *Front Cell Dev Biol* **9**, 652408 (2021).

69. Joglekar, A. et al. A spatially resolved brain region- and cell type-specific isoform atlas of the postnatal mouse brain. *Nat Commun* **12**, 463 (2021).

## FIGURE LEGENDS

**Figure 1. System for investigating the functional implications of maintaining low cell levels of p53.** A549 cells were cultured on multi-well chamber slides and the areas of interest were scanned. Cells were treated with scrambled siRNA or p53 siRNA in the presence or absence of various doses of MNNG, and the cell responses were monitored to generate live cell imaging videos. The videos were used for imaging and single-cell tracking, starting immediately after MNNG treatment. Progenitors were selected from the image designated as tracking time 0 min (T0), and the progenitors and their progeny were tracked empirically. Cell-lineage database comprised tracking results for one progenitor and their progeny, and any events that occurred in the cells. A cell-lineage map was generated from the database to represent the growth profile of a progenitor and its progeny through bipolar cell division (BD), multipolar cell division (MD), cell fusion (CF), and cell death (CD). If any progeny moved out from the areas of interest, data related to the lineage of that was not included in the cell-lineage database. Quantitative bioinformatics analysis was performed using the database, which was also used to develop a cell-fate simulation algorithm.

**Figure 2. Cell-population expansion rates determined by cell counting and single-cell tracking analysis.** Control (**a**) and p53 RNAi (**b**) cells were exposed to 1, 3, and 7 μM MNNG (Control and p53 RNAi cells exposed to those doses of MNNG are referred to as MNNG1, MNNG3, MNNG7, p53 RNAi-MNNG1, p53 RNAi-MNNG3 and p53 RNAi-MNNG7, respectively). (**a-f**) Images were divided into a 5 × 5 squares and cell population expansion curves were determined by counting the number of cells in a square (~ 512 × 512 pixels) at 1,000 min intervals (see Figure S5). Fifteen squares were selected from three independently generated videos. Expansion curves were compared as follows: Control vs. p53 RNAi (**c**), MNNG1 vs. p53 RNAi-MNNG1 (**d**), MNNG3 vs. p53 RNAi-MNNG3 (**e**), and MNNG7 vs. p53 RNAi-MNNG7 (**f**) cells. Student's *t*-test (**c-f**) and ordinary one-way ANOVA (Tukey's) (**a** and **b**) were performed (n=15), and standard errors are shown. Cell population expansion

curves of Control (**g**) and p53 RNAi (**h**) cells were determined using a cell-lineage database. Single-cell tracking was performed for 4,000 min with videos acquired at 10 min intervals (n = 399). The number of cells every 10 min was calculated and plotted. Growth curves were compared as follows: Control vs. p53 RNAi (**i**), MNNG1 vs. p53 RNAi-MNNG1 (**j**), MNNG3 vs. p53 RNAi-MNNG3 (**k**), and MNNG7 vs. p53 RNAi-MNNG7 (**l**) cells. (**i-l**) The data were analyzed by Student's *t*-tests in the following approach. The difference in cell numbers between n and n + 10 min was calculated (e.g. if the numbers of cells at 10 and 20 min were 100 and 103, the difference was 3). Because the total number of imaging points was 400, the 399 differences in time points can be calculated. Those differences for Control and p53 RNAi cells and those exposed to MNNG were used for the statistical analyses. (**a-f** and **i-l**) NS: non-significant, $^{*}P < 0.05$, $^{**}P < 0.01$, $^{***}P < 0.001$, $^{****}P < 0.0001$.

**Figure 3. Number of progeny produced from a progenitor.** (**a**) Example cell lineages are shown. If three cells derived from the same progenitor were found at 4,000 min, this cell lineage was grouped as A(1–3) and three were added to the total number of cells in group A(1–3). Similarly, if six cells derived from the same progenitor were found at 4,000 min, this lineage was grouped as B(4–6), and six were added to the total number of cells in Group B(4–6). Cells that underwent cell death were not represented by this analysis. (**b**) The total numbers of cells at 4,000 min in each group are shown.

**Figure 4. Analysis of multipolar cell division, cell death, and cell fusion using counting and single-cell tracking analysis.** Control and p53 RNAi cells were exposed to 1, 3, and 7 μM MNNG. The numbers of multipolar cell division (**a**) and cell death (**b**) events that occurred during the tracking time (4,000 min) were determined by counting of those events recorded in a video. Each time point of image was divided into four areas (Figure S6a), and three independently generated videos were used. Thus, counting was performed in 12 squares (n = 12). The numbers of multipolar cell division (**c**), cell death (**d**), and cell fusion (**e**) events that occurred during the tracking time (4,000 min) were determined using

single-cell tracking analysis (n = 335). (**a-e**) Statistical analysis was performed by ordinary one-way ANOVA (Tukey's). NS: non-significant, $^{*}P < 0.05$, $^{**}P < 0.01$, $^{***}P < 0.001$, $^{****}P < 0.0001$. Standard errors are shown.

**Figure 5. *In silico* generation of cell-lineage database to evaluate the impact of cell death on the cell population expansion.** (**a**) To evaluate the impact of cell death on population expansion, we created an *in silico* cell-lineage database, without cells undergoing cell death. In the example cell lineages, the number of survived cells was reduced by half as a result of cell death. If the siblings of the dead cell grew, the dead cell was assumed to continue to grow similar to its sibling, and a cell-lineage database was created *in silico* based on this assumption. (**b**) A cell population expansion curve was generated using the *in silico*-created cell-lineage database for Control and p53 RNAi cells (Control-Silico(-)cell death) and p53 RNAi-Silico(-)cell death, respectively). At a tracking time of 4,000 min, cell death resulted in a 7.4% reduction in the population size of p53 RNAi cells. The frequency of cell death (red lines) occurring during tracking is also shown. Statistical analysis was performed by ordinary one-way ANOVA (Tukey's). $^{*}P < 0.05$.

**Figure 6. Events leading to the induction of multipolar cell division.** (**a**) Cellular events that occurred prior to multipolar cell division were analyzed by tracing cell-lineages backwards. Pattern 1 (cell fusion (CF) ➛ multipolar cell division (MD)): cell fusion occurred prior to multipolar cell division. Pattern 2 (➛ MD): no cell fusion occurred. The numbers of each pattern occurring in 100 cell lineages are shown. Percentages of Patterns 1 and 2 in Control and p53 RNAi cells are also shown. (**b**) Cells that underwent multipolar cell division were identified. If the cells were generated by cell fusion, the origin of the fused cells was searched by tracing cell lineages backward. Pattern 3 (BD ➛ Sibling CF ➛ MD): bipolar cell division occurred, cells produced by division were fused, followed by

multipolar cell division. Pattern 4 (BD ➛ Non-Sibling CF ➛ MD): one sibling produced by bipolar cell division was fused with another non-sibling cell, followed by multipolar cell division. The numbers of each pattern in 100 cell lineages are shown. Percentages of Patterns 3 and 4 in Control and p53 RNAi cells are also shown. (**c**) Progeny produced by multipolar cell division were tracked and the number of reproductive progeny that underwent bipolar cell division was determined. The numbers of reproductive progeny found in 100 cell lineages and the percentages of such progeny among the total number of progeny produced by multipolar cell divisions are shown. (**d**) The number of multipolar cell division events was plotted against the number of bipolar cell division events. Numbers in (**d**) indicate doses of MNNG. (**a-d**) BD: bipolar cell division, MD: multipolar cell division, CD: cell death, and CF: cell fusion. Because the number of multipolar cell divisions in Control cells was low, we searched three videos to find multipolar cell divisions and then traced the cells back to their progenitors to determine the events preceding multipolar cell division. To normalize the values, we assumed that multipolar cell division occurred at a similar frequency to that recorded in the cell-lineage database.

**Figure 7. Schematic illustration of cell-fate simulation process.** (**a**) A cell lineage is composed of a progenitor and its progeny. Each of those cells is generated by a Start event (blue arrowhead), followed after a certain length of time by an End event (red arrowhead), such as bipolar cell division (BD), multipolar cell division (MD), cell death (CD), and cell fusion (CF). Cell-fate simulation was performed by combining these components. To perform the simulation, cells were classified based on the combination of the Start and the End events, e.g. BD-BD, and BD-MD (see Figure 7Sb for full list of classifications), and two sets of histogram data, referred to as Operation data-Events and Operation data-Time were created. (**b**) The Operation data-Events holds the frequency of events that occurred following a Start event e.g. BD, MD, or CF. In the case of the example shown in (**b**), if the Start event was BD, the histogram data indicated that the chances of the occurrence of each End event type, i.e.

BD, MD, CD, and CF, were ten, five, two, and three, respectively. In the example, MD and BD were selected from the histogram to assign an End event type to daughter cells produced by BD. Selection was performed by generating a random value. (**c**) Operation data-Time was then used to assign the length of time between the Start and End events using histogram data (Operation data-Time) for BD-BD and BD-MD, which included the choices of length of time. The processes was repeated to generate cell-lineage data for virtual cells.

**Figure 8. Operation modes.** (**a**) Standard mode: cell-fate simulation with one type of cell population performed with Operation data. (**b**) Dose simulation mode: Operation data created from other Operation data. The example in (**b**) represents an Operation data-Events, which holds information on the chance of the occurrence of subsequent events following an event, as outlined in Figure 7c. In the case of Operation data A, generated from a cell-lineage database created by tracking cells exposed to an ×2 dose of a drug, ten, five, two, and four bipolar cell division (BD), multipolar cell division (MD), cell death (CD), and cell fusion (CF) events, respectively, were assumed to occur following the event. On the other hand, Operation data B, generated from a cell-lineage database created by tracking cells in another cell population exposed to a ×5 dose of a drug, assumed that one, five, four, and ten BD, MD, CD, and CF events would occur following the same type of events referred in Operation A. If a cell population was assumed to be exposed to a ×3 dose of a drug, Operation data for the exposed cells can be created by calculating e.g. BD (7) = BD for Operation data A (10) + [(Operation data B (1) − Operation data A (10)/(Dose 2 (×5) − Dose 1 (×2))) × (Intermediate dose (×3) − Dose 1 (×2)). A similar calculation can be performed for all data stored in Operation data-Time and -Events to create new Operation data (Operation data-virtual). Using the Operation data, the fate of cells could be simulated without the need for empirical analysis. (**c**) Mixed culture mode: assuming that multiple cell types coexist in a culture, simulation is performed using corresponding Operation data for each cell type. (**d**) Sequential mode: cell-fate simulation is performed with Operation data and then switched to

another Operation data. If the second Operation data is for cells treated with a drug, this simulation allows the effect of drug treatment to be evaluated virtually. (**e**) Mixed culture-Sequential mode: this mode is a combined Mixed culture (**c**) and Sequential (**d**) mode.

**Figure 9. Simulations of effects of p53 silencing and MNNG exposure on cell population expansion.** Simulations were performed using Operation data generated from cell-lineage data with a total of 5,000 virtual progenitors for a simulation time of 15,000 min. (**a** and **b**) Virtual cell population expansion curves of Control-Sim cells and cells exposed to various doses of MNNG (**a**: 0–4,000 min, and **b**: whole scale, 0–15,000 min). (**c**, **d**, **e**, and **f**) Data obtained from the simulation were compared with growth curves determined by single-cell tracking analysis; (**c**) Control, (**d**) MNNG1, (**e**) MNNG3, and (**f**) MNNG7. Difference (%) was determined by obtaining the sum of the number of cells (single-cell tracking)/the number of Simulated cells determined at each simulation time point divided by 1,500 simulation time × 100. For example, a difference of 2.7% implied that the simulation generated 2.7% more cells compared with the single-cell tracking data. (**g** and **h**) Virtual cell growth curves of p53 RNAi-Sim cells and cells exposed to various doses of MNNG (**g**: 0–4,000 min, and **h**: whole scale, 0–15,000 min). (**i**, **j**, **k**, and **l**) These simulation data were compared with the cell population expansion curves determined by single-cell tracking analysis; (**i**) p53 RNAi, (**j**) p53 RNAi-MNNG1, (**k**) p53 RNAi-MNNG3, and (**l**) p53 RNAi-MNNG7. Results of simulation obtained using Operation data-p53 RNAi-Silico(-)cell death were also included in **g** and **h**.

**Figure 10. Virtual dose-response analysis.** Virtual Operation data corresponding to each 0.5 µM dose of MNNG was generated in Dose simulation mode. (**a and b**) Virtual MNNG-dose-response cell growth curves of Control and p53 RNAi cells generated by the simulation using Operation data-Control to MNNG 1.5 (purple), 2–3 (pink), 3.5–6.5 (dark green), and 7 (marron) are shown. (**c**) The numbers of cells at simulation times of 4,000 min (indicated by a blue arrow in (**a**) and (**b**)) were plotted. Results of

single-cell tracking analysis are also included. (**d**) The numbers of cells at simulation times of 15,000 min (indicated by a red arrow in (**a**) and (**b**)) were plotted. The difference of cell number between Control cells and the cells exposed to 7 μM MNNG, and p53 RNAi cells and the cells to the dose of MNNG are shown (Italic). The number of cells at 0 and 15,000 min were also shown. (**c** and **d**) Standard deviations are shown. A natural log scale was used. (**e**) Time necessary to reach a cell population to be doubled (100 to 200 cells) was determined by using Operation data-Control, MNNG7, p53 RNAi, and p53 RNAi-MNNG7. The difference in time between MNNG7-Sim (9,651 min) and Control-Sim (2,501 min) was 7,150 min. Similarly, the difference in doubling time between p53 RNAi-MNNG7-Sim and p53 RNAi-Sim was 4,510 min. Assuming that the difference in doubling time between MNNG7-Sim and Control-Sim represents the effect of MNNG induced by e.g. DNA breaks and p53-mediated responses, while that between p53 RNAi-MNNG7-Sim and p53 RNAi-Sim only represents the effect of MNNG induced by e.g. DNA breaks, 63% and 37% of growth suppression in MNNG7-Sim were likely to be due to the effect of MNNG caused by e.g. DNA breaks and responses induced by the stabilization of p53, respectively.

**Figure 11. Simulation of growth of the progeny of multipolar cell division.** The simulation was performed using Operation data-Control and p53 RNAi in Standard mode. (**a**) The progeny of multipolar cell division and those that underwent bipolar cell division were indicated in burgundy and green, respectively. The simulation was carried out for 2,500 progeny, which generated $6.6 \times 10^6$ cells during the 20,000 min of simulation. (**b** and **c**) Whole-scale and magnified images generated by the simulation using the Operation data-Control are shown in (**b**) and (**c**), respectively. (**d**) An animation was created to visualize the growth of the cells (Figure 11-video 1) and an image at simulation time 20,000 min is shown. Dots of grey, burgundy and green, represent cells that underwent bipolar division, multipolar division and multipolar division followed by bipolar division, respectively. (**e** and **f**) Whole-scale and magnified images generated by the simulation using Operation data-p53 RNAi are shown in

(**e**) and (**f**), respectively. (**g**) An animation was created to visualize the growth of the cells (Figure 11-video 2) and an image at simulation time 20,000 min is shown. Bipolar cell division (BD), multipolar cell division (MD), and multipolar cell division followed by bipolar cell division (MD-BD).

**Figure 12. Limiting expansion of p53 RNAi cells in a Control cell population.** We simulated the expansion of the p53 RNAi cell population (4% at the initial time point) in a Control cell population (96% at the initial time point) using Mixed culture mode with Operation data-Control and p53 RNAi for a simulation time of 20,000 min with 500 progenitors and repeating 10 simulations (total 5,000 progenitors). (**a**) Simulation of 480 Control progenitors was carried out using Operation data-Control and 20 p53 RNAi progenitors with Operation data-p53 RNAi. The initial percentage of p53 RNAi cells was 4%, which was reduced to 2.4% at 20,000 min. (**b**) The sums of multipolar cell division, cell death, and cell fusion events (MD+CD+CF) are shown. (**c**) Simulation was performed using Operation data-p53 RNAi-Silico(-)cell death.

**Figure 13. Expansion of p53 RNAi cells in a Control cell population subjected to virtual MNNG exposure.** We simulated the response of p53 RNAi cells in a Control cell population to MNNG exposure using Mixed culture-Sequential mode. (**a**) The simulation was performed with 96% Control and 4% p53 RNAi cells, using Operation data-Control and p53 RNAi for 9,900 min. The Operation data was then switched to e.g. MNNG7 and p53 RNAi-MNNG7 for virtual MNNG treatment, and the simulation was continued up to 20,000 min. In the animation (Figure 13-videos 1), the pixel value of the image was reduced to indicate the virtual MNNG treatment. (**b-f**) In the simulation, Operation data corresponding to (**b**) 1.5, (**c**) 3, (**d**) 5, (**e**) 6, and (**f**) 7 μM MNNG were used to perform a virtual MNNG treatment. The numbers in the images indicate the percent of p53 RNAi cells at simulation times 0 and 20,000 min. (**g**) The percentages of p53 RNAi cells in the population were plotted. Statistical analysis (n=10) was performed using data at simulation time 20,000 min by ordinary one-way ANOVA. NS:

nonsignificant, $^{*}P < 0.05$, $^{****}P < 0.0001$. (**h**) Based on the simulation data for 7 µM MNNG, percentage of p53 RNAi cells following repeated 7 µM MNNG exposure every 10,000 min (~7days) was calculated. Arrows indicate the time that the virtual exposure was performed.

**Figure 14. Role of the low levels of p53 in suppression of multipolar cell division, cell death, cell fusion, and damage response.** (**a**) Characteristics of Control and p53 RNAi cells. (**b**) The simulation of the fate of p53 RNAi cells in the Control cell population. (**c**) The simulation of the fate of p53 RNAi cells in the Control cell population, which were virtually exposed to 7 µM MNNG. The percentage of aneuploid cells is also shown.

## SUPPLEMENTARY FIGURES

**Figure 1-figure supplement 1. Events occurring in the cells.** Cellular events that occurred in A459 cells were categorized as follows: bipolar cell division, tripolar cell division, tetrapolar cell division, cell death, and cell fusion. In the current study, tripolar and tetrapolar cell divisions were defined as multipolar cell division. Green arrowheads indicate cells that underwent an event. Red arrowheads indicate daughter cells, a dead cell, and a fused cell. Timestamps (min) relative to the first frame and a scale bar (20 μm) are shown. Corresponding videos are deposited in Dryad.

**Figure 1-figure supplement 2. Cell growth condition.** (**a**) Cell density and average cell size every 10 min were plotted. (**b**) Cell density maps were created using a heat map scale. Still images were taken from Figure 1-video 1. Timestamps (min) and a scale bar (80 μm) are shown. (**c**) The cell positions that were determined using single-cell tracking and recorded in the cell-lineage database were used. Cell density map created by assigning value 1 to a pixel within the 20-pixel diameter area from the position of a cell (blue); if an area overlapped with other areas, the pixel was assigned the sum of the number of overlapped areas (light green). At the high cell density area, values were increased according to the number of overlaps, allowing to generate a heat map. These values were used to generate heat maps.

**Figure 1-figure supplement 3. Determination of minimum number of cell-lineages required to build a cell-lineage database.** A cell-lineage database containing 50–240 cell-lineages was used to determine cell population expansion curves. Cell-lineage database was created by tracking of 485 progenitors of Control cells. (**a-e**) Cell population expansion curves determined by randomly selecting 50 (**a**), 80 (**b**), 120 (**c**), 140 (**d**), and 240 (**e**) cell-lineages from the cell-lineage database. The number of cells every 10 min was calculated and plotted. The random selection was repeated three times (green,

orange, and red lines) to show variations at a tracking time of 4,000 min (black bars). Each repeated selection was performed in a way that the same lineage was not selected, except for the selection of 240 lineages. The initial number of cell-lineages was normalized to 100. (**f**) Variations of 4,000 min were plotted.

**Figure 1-figure supplement 4. Accumulation of particles following siRNA transfection and analysis of p53 expression following transfection and/or MNNG exposure.** (**a**) Particles formed following siRNA transfection are shown. DIC and objects with pixel value 150–254 and size 5–30 pixels were extracted from the DIC image (Particles). (**b**) The numbers of particles at five different locations in the image were plotted. Blue lines represent the average number of particles at each time point per location and the red line shows the overall average. MNNG treatment was performed after approximately 1,740 min of siRNA transfection, and continued for 30 min. The number of particles peaked at 3,750 min after transfection. Single-cell tracking was started immediately after MNNG treatment and continued for 4,000 min. (**c**) Western blotting with anti-p53 antibody was performed 48 h after siRNA treatment. Amounts of p53 relative to Control are shown.

**Figure 2-figure supplement 1. Determination of cell-population expansion rate using video images.** A video image (typically 2,560 pixels × 2,560 pixels) was divided into 5 × 5 squares and the numbers of cells in selected squares were counted. Counting was performed every 1,000 min in video images from 0–4,000 min.

**Figure 4-figure supplement 1. Counting multipolar cell division and cell death using live-cell imaging videos.** (**a**) Each time point of the video image was divided into four squares, and cell death and multipolar cell division in each square were marked to determine the numbers of those events that occurred during imaging. Three independently generated videos were used, and 12 squares were thus

counted. The positions of multipolar cell division and cell death were also stacked to generate multipolar cell division and cell death density maps. Multipolar cell division (**b**) and cell death (**c**) density maps were created using a similar approach to cell density determination (Figure S2b). Density was shown using a heat map scale. Black squares correspond to the area used for single-cell tracking.

**Figure 7-figure supplement 1. Cell-fate simulation algorithm.** Outlines of the cell fate simulation algorithm are shown. (**a**) Overall summary of the algorithm, (**b**) creation of Operation data and its types, (**c**) simulation arrays and its format, (**d**) initial event assignment, (**e**) initial cell-lineage database generation, (**f**) main event assignment, (**g**) re-assignment of events in cases with cell fusion, (**h**) cell-lineage database generation, and (**i**) trimming of cell-lineage data ends to switch from the first to second Operation data. Bipolar cell division (BD), multipolar cell division (MD), cell death (CD), cell fusion (CF), and no cell division (NonDiv).

**Figure 7-figure supplement 2. Single-cell tracking and cell-fate simulation processes.** (**a**) Overall scheme of single-cell tracking. **(b)** Processes of cell-fate simulation.

**Figure 7-figure supplement 3. Cell-lineage maps generated by single-cell tracking and a cell-fate simulation algorithm.** (**a**) Cell-lineage maps generated by cell-lineage database Control cells. The single-cell tracking analysis created 335 cell-lineage datasets, and 16 cell-lineage maps are shown. (**b**) Cell-lineage maps generated by simulation using Operation data-p53 RNAi. The simulation created 2,500–5,000 virtual cell-lineage datasets, and 16 cell-lineage maps generated from the virtually created cell-lineage datasets are shown. Light blue circle, mitosis; pink square, cell death; orange circle and orange vertical line, cell fusion; black vertical line, bipolar cell division; red vertical line, multipolar cell division.

**Figure 8-figure supplement 1. Determination of number of progenitors required to perform a reproducible simulation.** The simulation was performed with 300–2,000 progenitors using either the Operation data-Control (**a**) or Operation data-MNNG7 (**b**). Each simulation was repeated five times and virtual cell-lineage databases for Control-Sim and MNNG7-Sim cells were created to determine the population expansion curves of the virtual cells. The percentage of variation relative to the average at simulation time 15,000 min is also shown.

**Figure 9-figure supplement 1. Cell-doubling time distribution.** Cell-doubling time distribution was determined using the cell linage database generated by single-cell tracking and simulation data. (**a**, **b**, **c**, and **d**) Cell doubling times of (**a**) Control, (**b**) MNNG1, (**c**) MNNG3, and (**d**) MNNG7 cells determined using the cell-linage database. (**e, f, g** and **h)** Simulations were performed using the Operation data (**e**) Control, (**f**) MNNG1, (**g**) MNNG3, and (**h**) MNNG7. (**i**, **j**, **k**, and **l)** Cell doubling time of (**i**) p53 RNAi, (**j**) p53 RNAi-MNNG1, (**k**) p53 RNAi-MNNG3, and (**l**) p53 RNAi-MNNG7. (**m**, **n**, **o**, and **p)** Results of corresponding simulations are shown; the Operation data (**m**) p53 RNAi, (**n**) p53 RNAi-MNNG1, (**o**) p53 RNAi-MNNG3, and (**p**) p53 RNAi-MNNG7. Arrow indicates the average cell-doubling time, and the average cell-doubling times are shown.

**Figure 9-figure supplement 2. Simulations of multipolar cell division, cell death, and cell fusion.** The numbers of multipolar cell division (**a**), cell death (**b**), and cell fusion (**c**) events in a virtual cell population generated by the simulation were compared with those determined by single-cell tracking analysis. The simulation was performed with 1,000 progenitors for a simulation time of 15,000 min and was repeated 10 times. The range of results obtained by the simulation is also indicated.

## SUPPLEMENTARY VIDEOS

**Figure 1-video 1. Visualization of cell density.** Density of cultured cells visualized using a heat map color scale. Timestamps (min) and a scale bar (80 μm) are shown.

**Figure 1-video 2. Visualization of progress of transfection.** DIC and particles with 150–255 grayscale and size of 5–30 pixels are shown. Timestamps (min) and a scale bar (20 μm) are shown.

**Figure 11-video 1. Cell-fate simulation of progeny of multipolar cell division in Control cells.** Progeny of multipolar cell division and the progeny that underwent bipolar cell division are indicated in burgundy and green, respectively. Other cells are indicated in gray. The animation video was created using data from the virtual cell-lineage database and Operation data-Control. After assigning the initial positions of the cells, the cell movement was created programmatically. When cell death occurred, virtual cells were split into small particles.

**Figure 11-video 2. Cell-fate simulation of progeny of multipolar cell division in p53 RNAi cells.** Progeny of multipolar cell division and the progeny that underwent bipolar cell division are indicated in burgundy and green, respectively. Other cells are indicated in gray. The animation video was created using data from the virtual cell-lineage database and Operation data-p53 RNAi. After assigning the initial positions of the cells, the cell movement was created programmatically. When cell death occurred, virtual cells were split into small particles.

**Figure 12-video 1. Cell-fate simulation of p53 RNAi cells in a Control cell population.** The p53 RNAi cells are indicated in blue. Other cells are indicated in gray. The animation video was created

using data from the virtual cell-lineage database and Operation data-Control and p53 RNAi. After assigning the initial position of the cells, cell movement was created programmatically. When cell death occurred, virtual cells were split into small particles.

**Figure 13-video 1. Cell-fate simulation of p53 RNAi cells in a Control cell population subjected to virtual MNNG treatment.** The p53 RNAi cells are indicated in blue. Other cells indicated in gray. The animation video was created using data from the virtual cell-lineage database and Operation data-Control and p53si, and MNNG7 and p53 RNAi-MNNG7. The pixel value of the image was changed after virtual MNNG treatment at a simulation time of 10,000 min. After assigning the initial position of the cells, cell movement was created programmatically. When cell death occurred, virtual cells were split into small particles.

## SOURCE DATA

**Figure 1-source data 1. Cell growth condition.**

The data was used in Figure 1-figure supplement 2.

**Figure 1-source data 2. Determination of minimum number of cell-lineages required to build a cell-lineage database.**

The data was used in Figure 1-figure supplement 3.

**Figure 1-source data 3. Accumulation of particles following siRNA transfection and analysis of p53 expression following transfection and/or MNNG exposure.**

The data was used in Figure 1-figure supplement 4.

**Figure 2-source data 1. Cell-population expansion rates determined by cell counting and single-cell tracking analysis.**

The data was used in Figure 2.

**Figure 3-source data 1. Number of progeny produced from a progenitor.**

The data was used in Figure 3.

**Figure 4-source data 1. Analysis of multipolar cell division, cell death, and cell fusion using counting and single-cell tracking analysis.**

The data was used in Figure 4.

**Figure 5-source data 1. *In silico* generation of cell-lineage database to evaluate the impact of cell death on the cell population expansion.**

The data was used in Figure 5.

**Figure 6-source data 1. Events leading to the induction of multipolar cell division.**

The data was used in Figure 6.

**Figure 8-source data 1. Determination of number of progenitors required to perform a reproducible simulation.**

The data was used in Figure 8-figure supplement 1.

**Figure 9-source data 1. Simulations of effects of p53 silencing and MNNG exposure on cell population expansion.**

The data was used in Figure 9.

**Figure 9-source data 2. Cell-doubling time distribution.**

The data was used in Figure 9-figure supplement 1.

**Figure 9-source data 3. Simulations of multipolar cell division, cell death, and cell fusion**.

The data was used in Figure 9-figure supplement 2.

**Figure 10-source data 1. Virtual dose-response analysis.**

The data was used in Figure 10.

**Figure 11-source data 1. Simulation of growth of the progeny of multipolar cell division.**

The data was used in Figure 11.

**Figure 12-source data 1. Limiting expansion of p53 RNAi cells in a Control cell population.**

The data was used in Figure 12.

**Figure 13-source data 1. Expansion of p53 RNAi cells in a Control cell population subjected to virtual MNNG exposure.**

The data was used in Figure 13.

# Figure 1

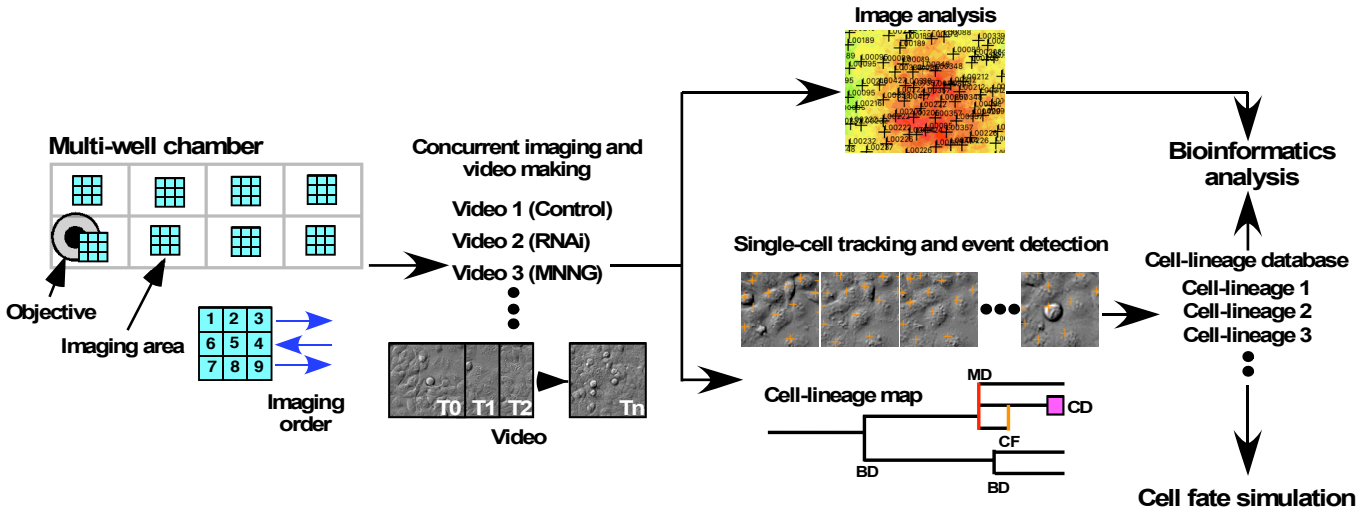


Rancourt et al.

# Figure 2

## Cell counting

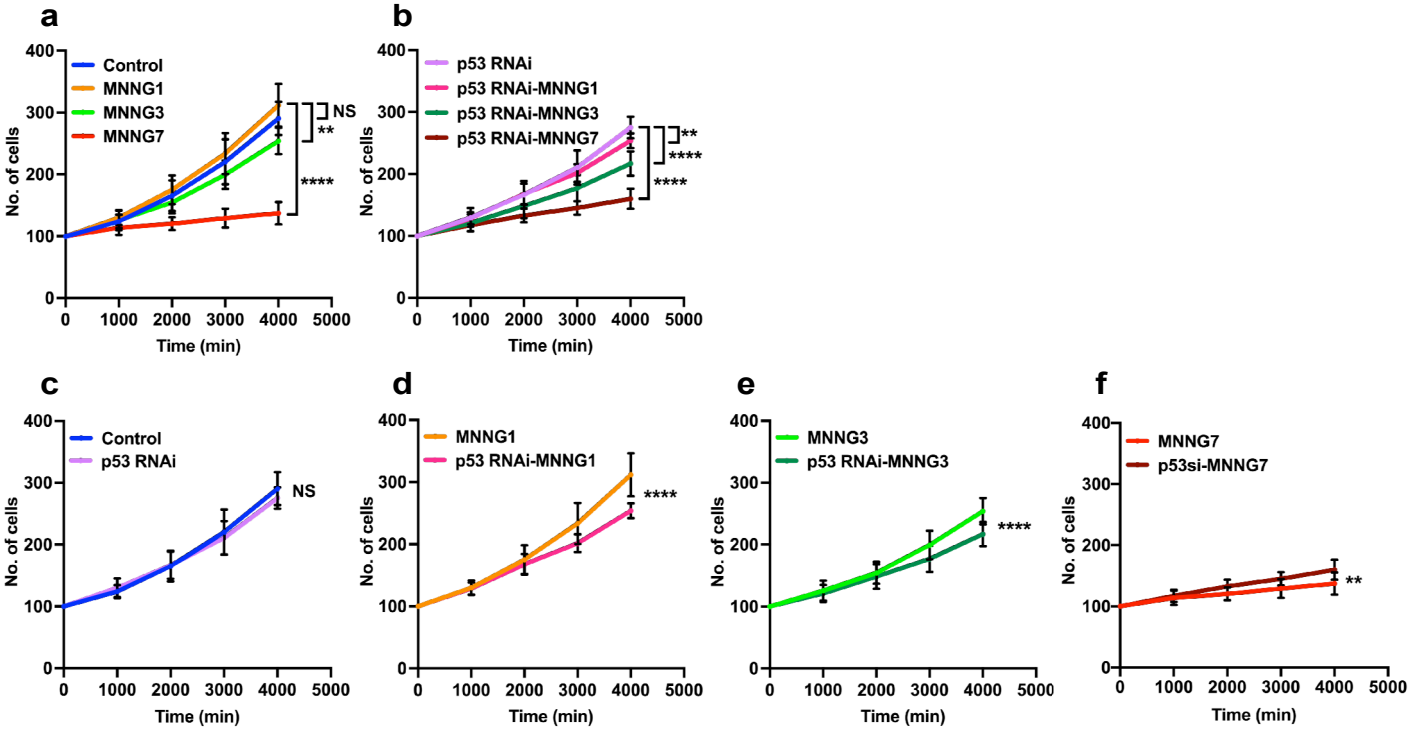


## Single-cell tracking

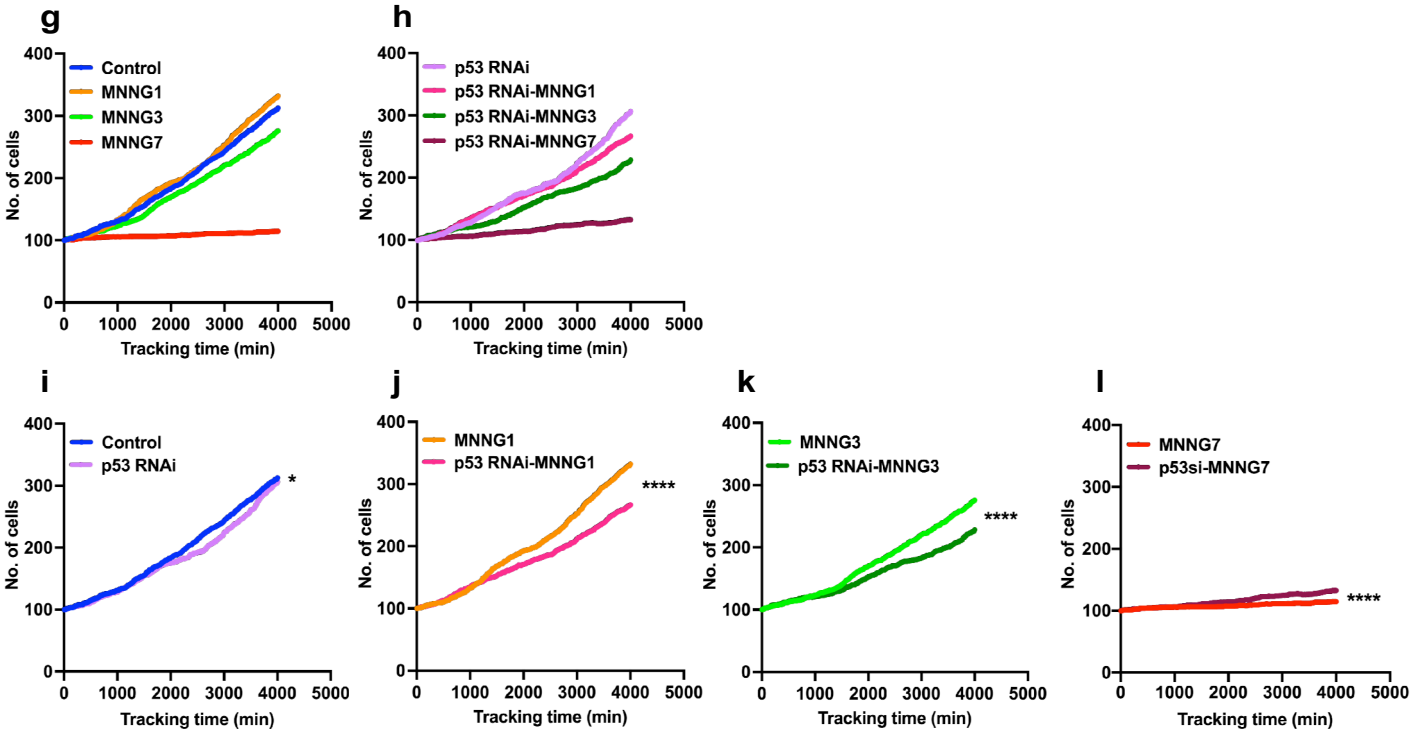


Rancourt et al.

# Figure 3

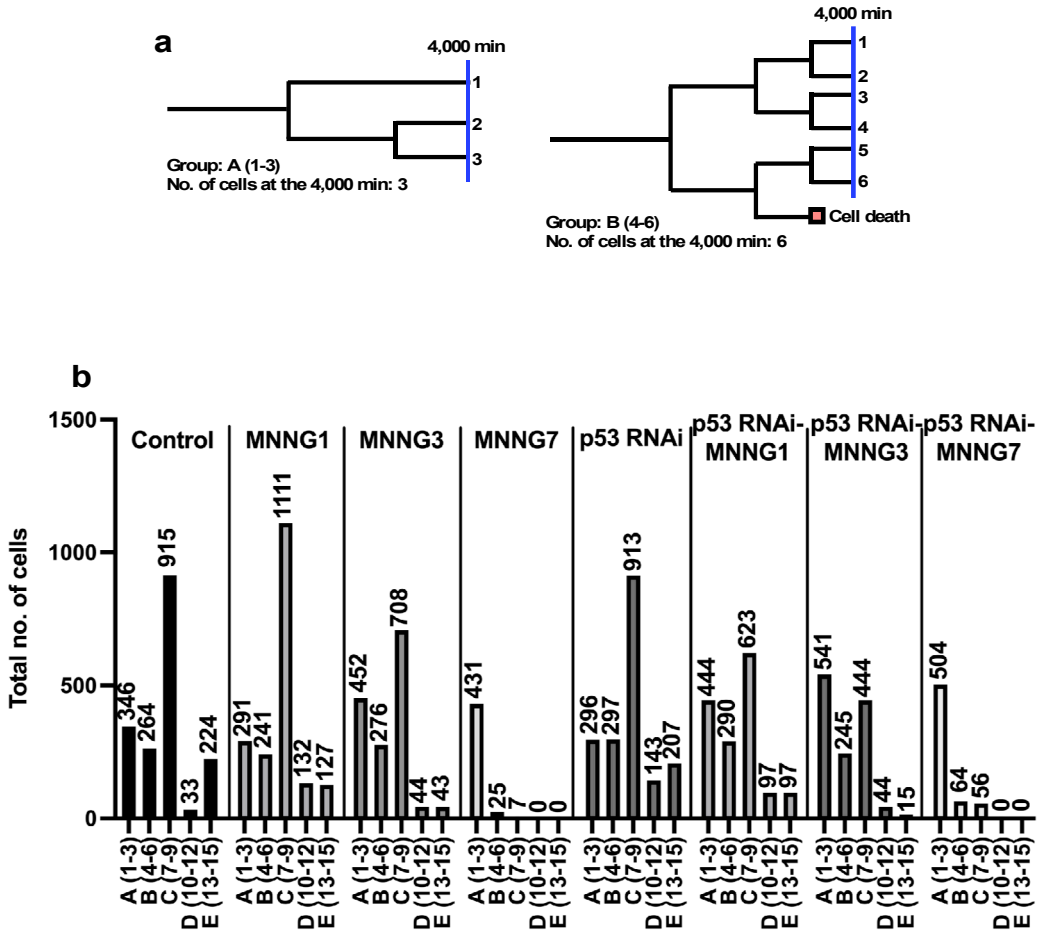
a
4,000 min
1
2
3
Group: A (1-3)
No. of cells at the 4,000 min: 3
4,000 min
1
2
3
4
5
6
Cell death
Group: B (4-6)
No. of cells at the 4,000 min: 6
b
Total no. of cells
1500
1000
500
0
Control
MNNG1
MNNG3
MNNG7
p53 RNAi
p53 RNAi-MNNG1
p53 RNAi-MNNG3
p53 RNAi-MNNG7
346
264
915
33
224
291
241
1111
132
127
452
276
708
44
43
431
25
7
0
0
296
297
913
143
207
444
290
623
97
97
541
245
444
44
15
504
64
56
0
0
A (1-3)
B (4-6)
C (7-9)
D (10-12)
E (13-15)

# Figure 4

## Counting of multipolar cell division and cell death

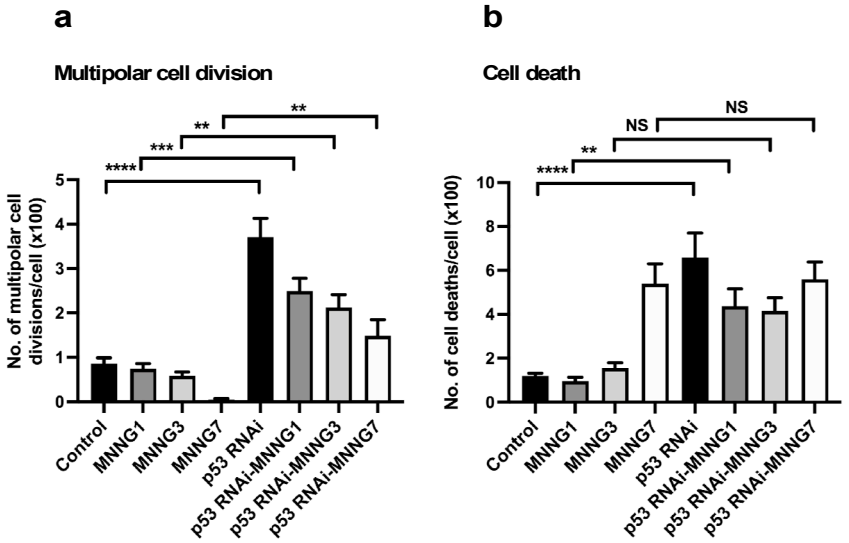


## Sinle-cell tracking

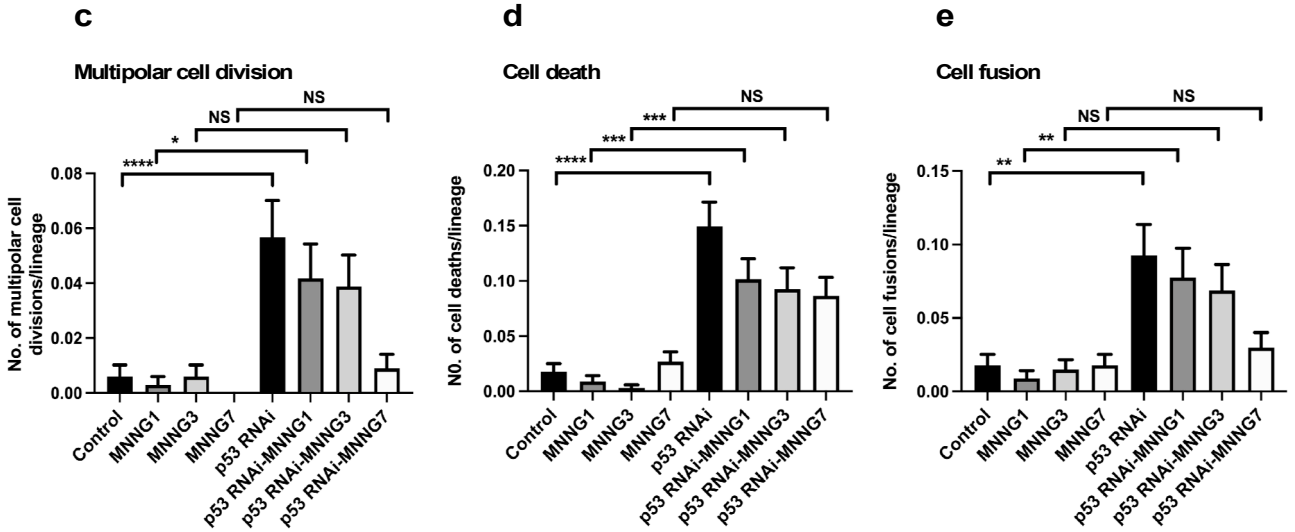


Rancourt et al.

# Figure 5

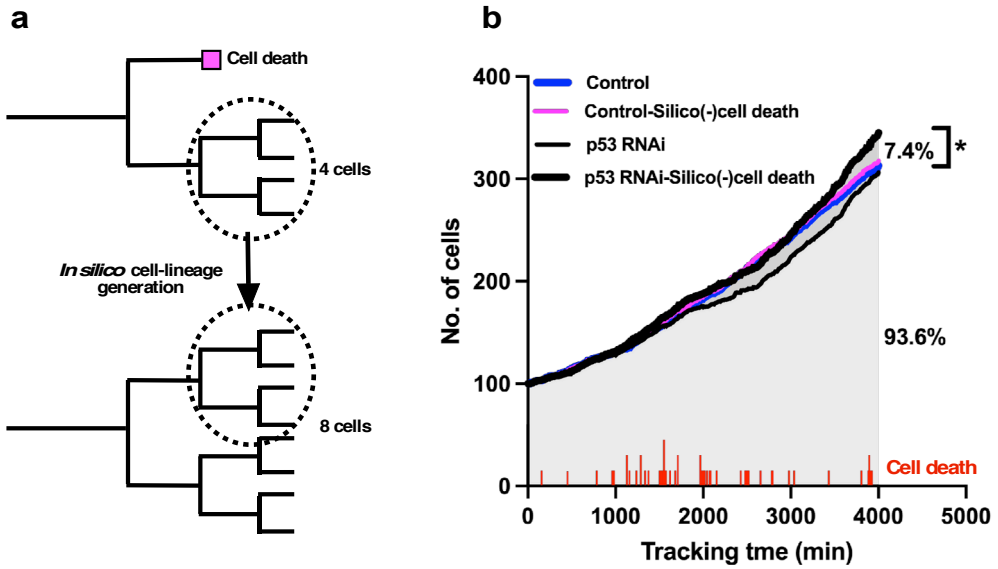


Rancourt et al.

# Figure 6

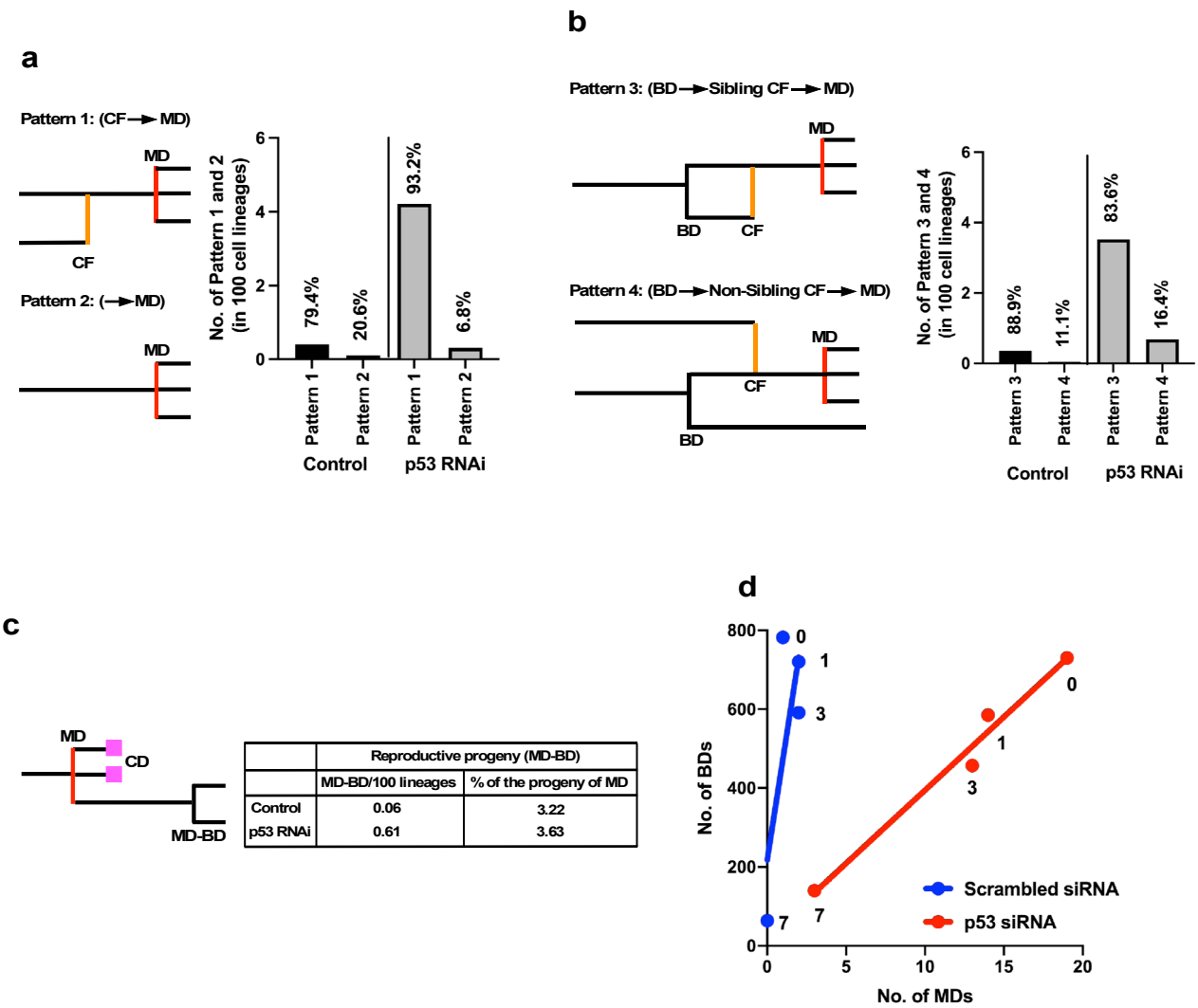


| | Reproductive progeny (MD-BD) | |
|---|---|---|
| | MD-BD/100 lineages | % of the progeny of MD |
| Control | 0.06 | 3.22 |
| p53 RNAi | 0.61 | 3.63 |

Rancourt et al.

# Figure 7

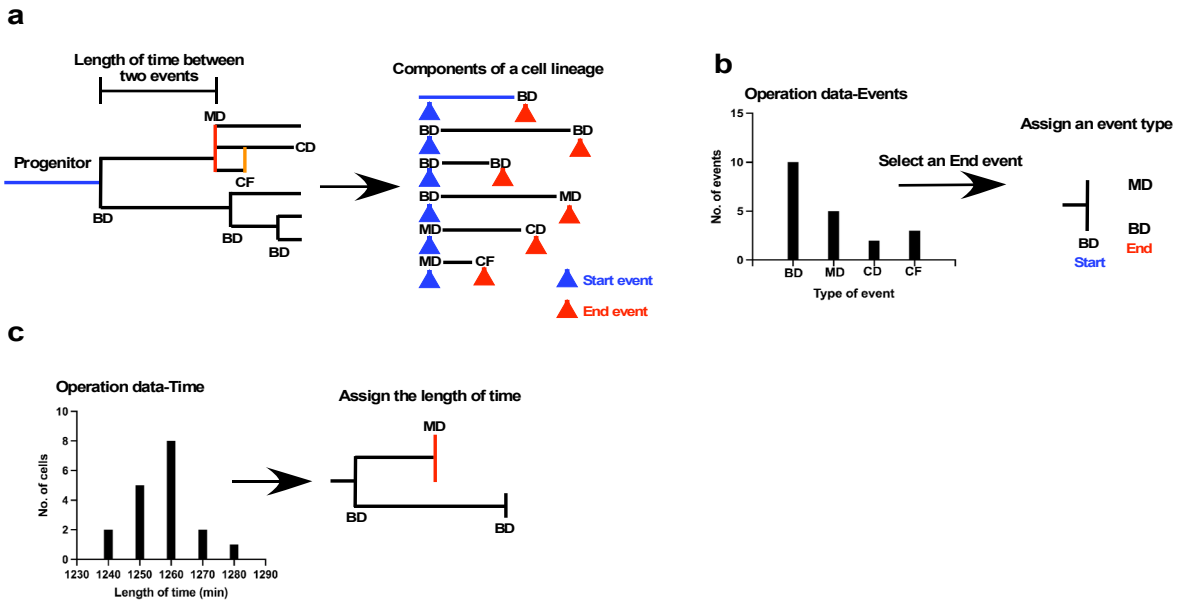


Rancourt et al.

# Figure 8

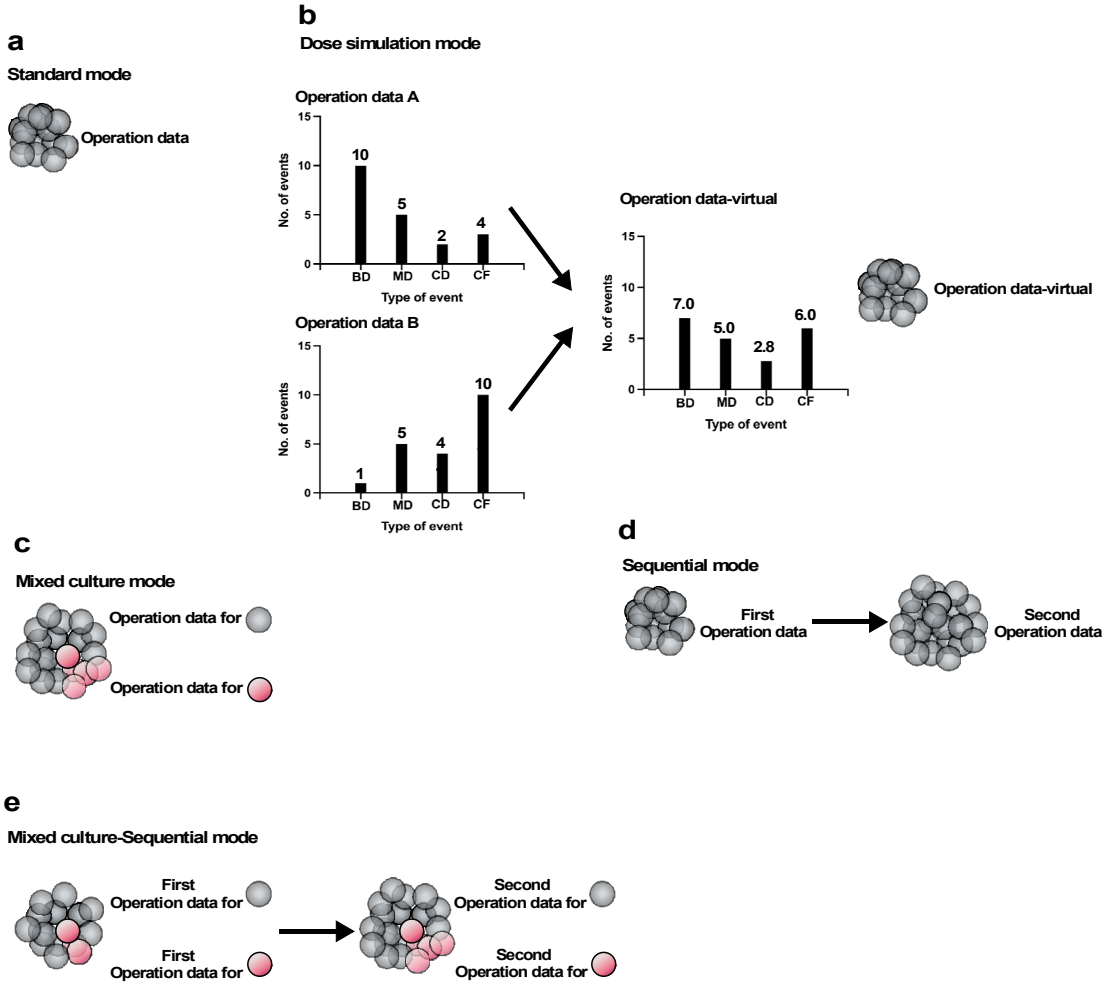





Rancourt et al.

# Figure 9

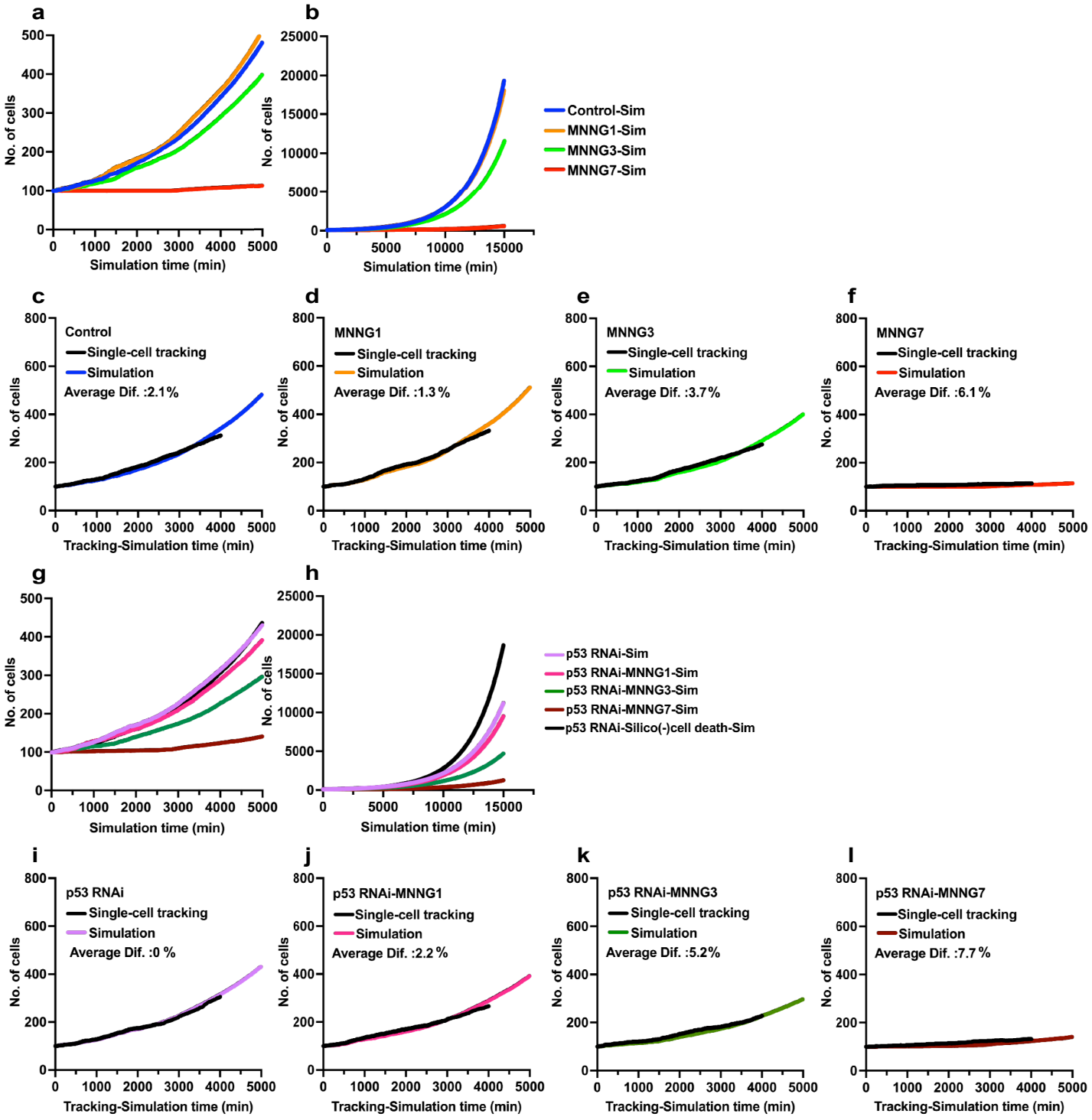


Rancourt et al.

# Figure 10

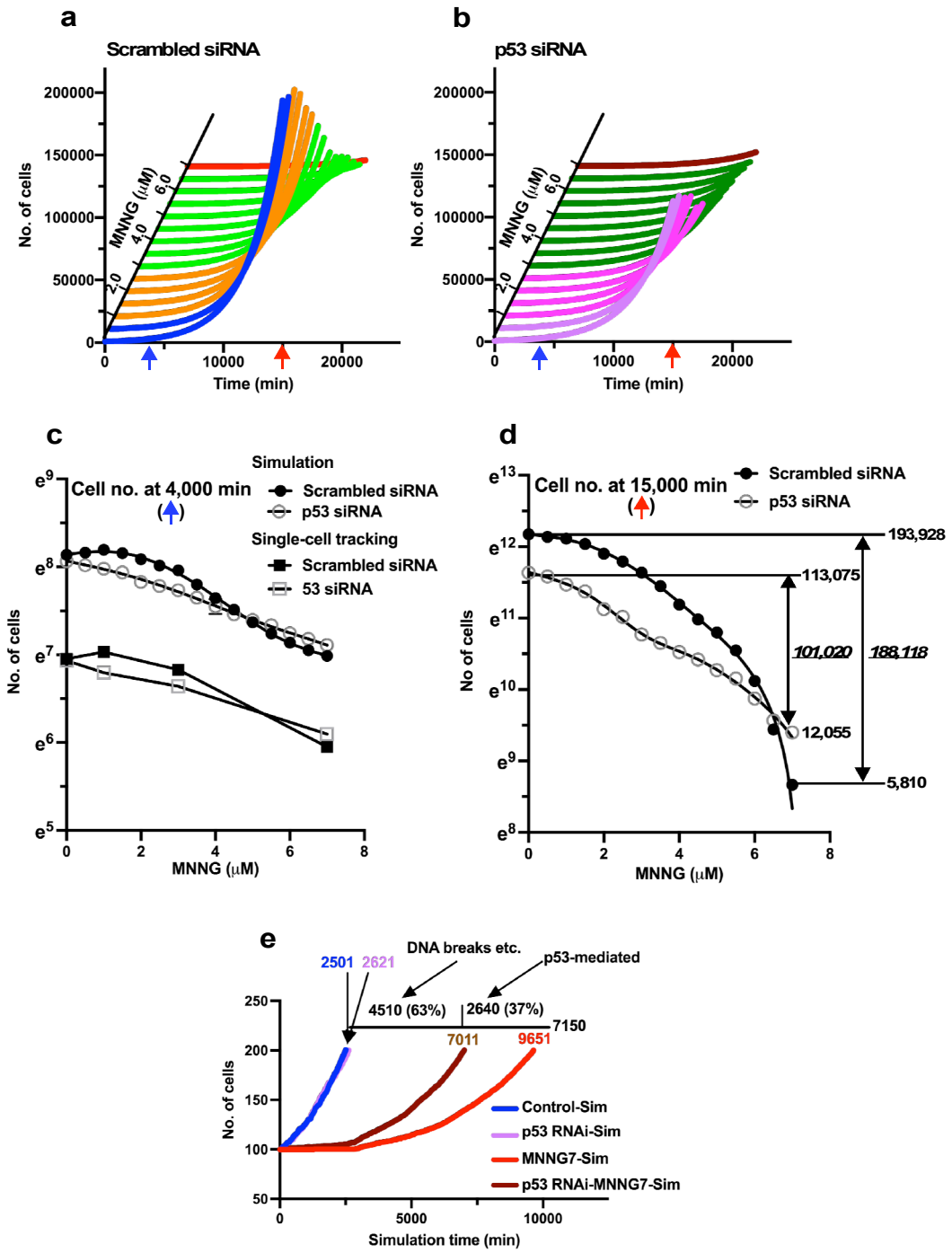


Rancourt et al.

# Figure 11

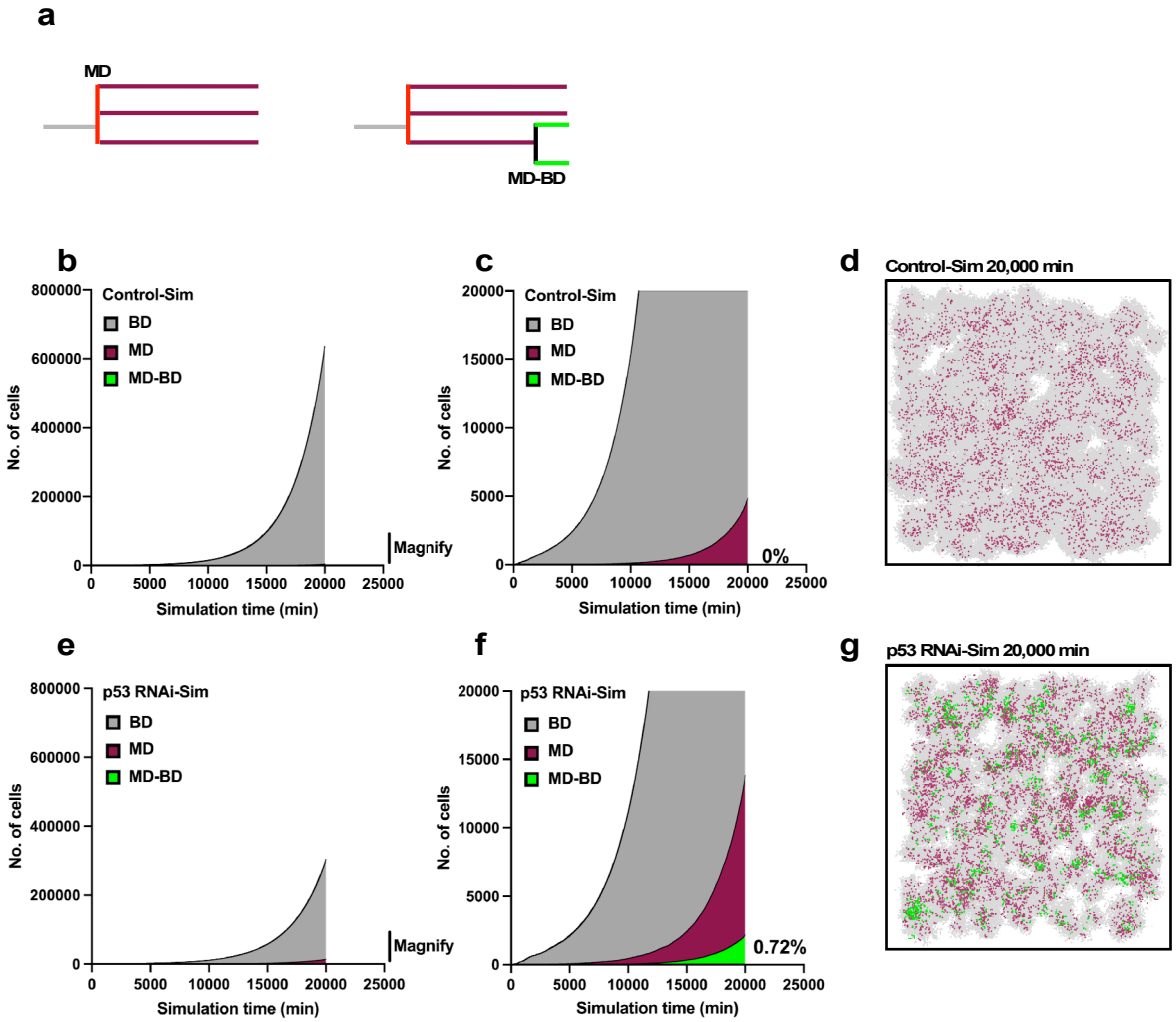


Rancourt et al.

# Figure 12

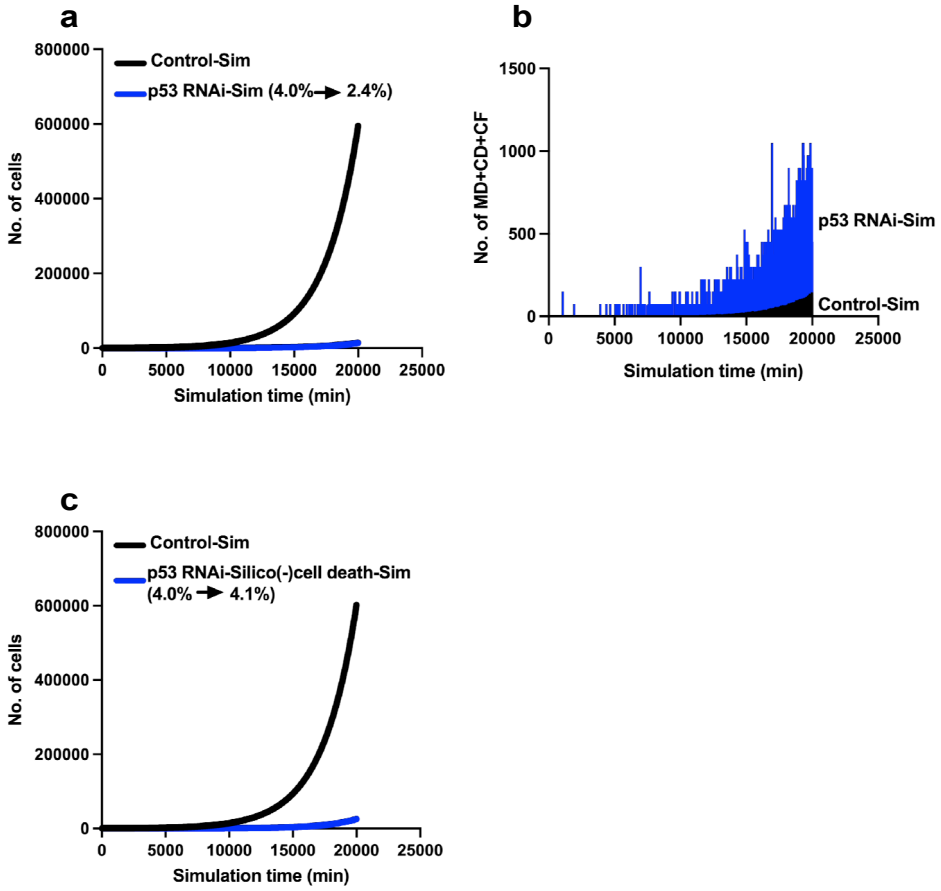


Rancourt et al.

# Figure 13

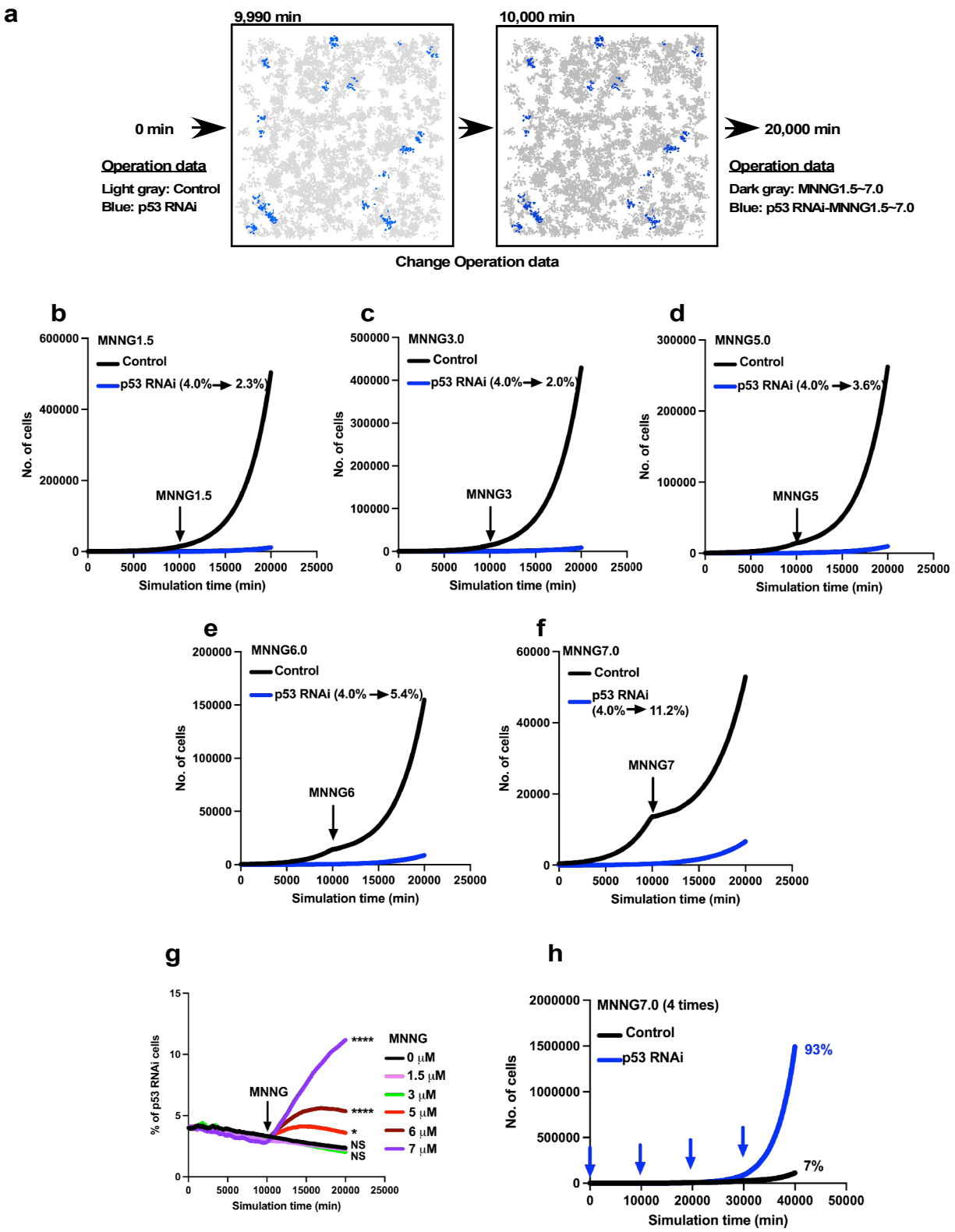


Rancourt et al.

# Figure 14

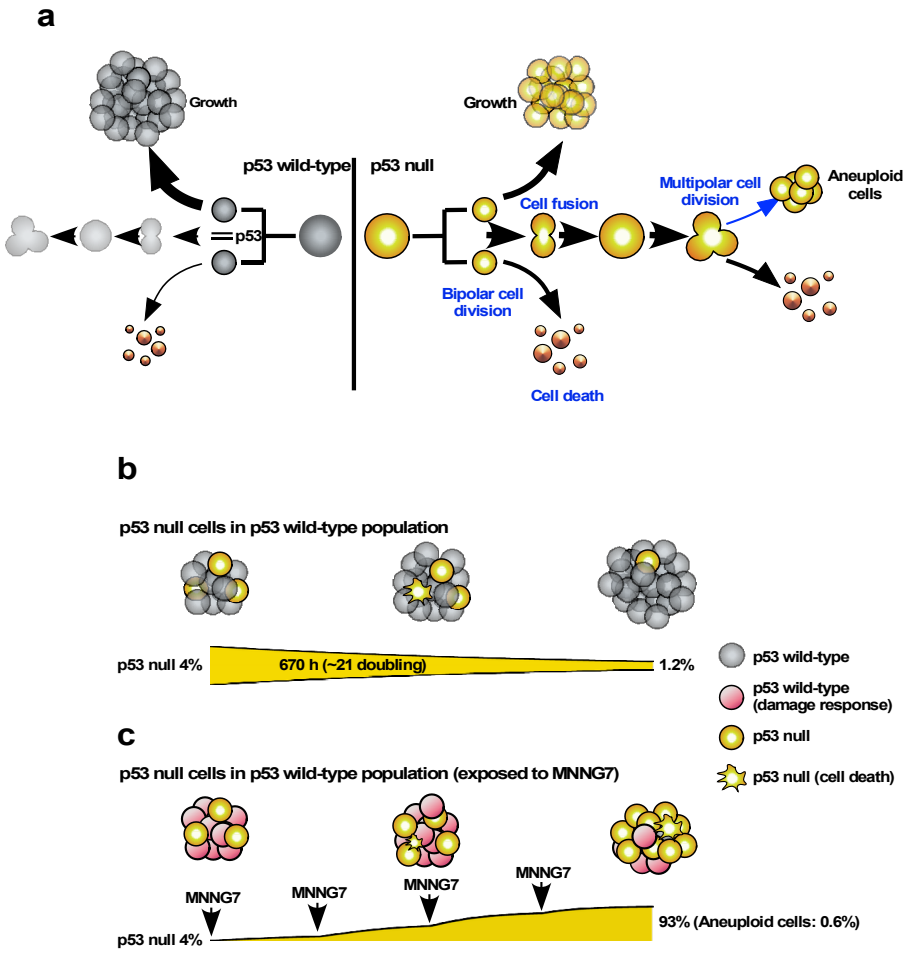


Rancourt et al.